Barozh 12: Formation processes of a late Middle Paleolithic open-air site in western Armenia

Phil Glauberman [a, b, *], Boris Gasparyan [a], Jennifer Sherriff [c], Keith Wilkinson [d], Bo Li [e, f], Monika Knul [d], Alex Brittingham [g], Michael T. Hren [h], Dmitri Arakelyan [i], Samvel Nahapetyan [j], Yannick Raczynski-Henk [k], Hayk Haydosyan [a], Daniel S. Adler [g]

[a] Institute of Archaeology and Ethnography, National Academy of Sciences of the Republic of Armenia, Yerevan, Armenia
[b] Humanities and Social Sciences Cluster, Xi'an Jiaotong-Liverpool University, Suzhou, China
[c] Department of Geography, Royal Holloway University of London, Egham, United Kingdom
[d] Department of Archaeology, Anthropology and Geography, University of Winchester, Winchester, United Kingdom
[e] Centre for Archaeological Science, School of Earth, Atmospheric and Life Sciences, University of Wollongong, Wollongong, New South Wales, Australia
[f] Australian Research Council (ARC) Centre of Excellence for Australian Biodiversity and Heritage, University of Wollongong, Wollongong, New South Wales, Australia
[g] Department of Anthropology, Old World Archaeology Program, University of Connecticut, Storrs, CT, USA
[h] Department of Geosciences, University of Connecticut, Storrs, CT, USA
[i] Institute of Geological Sciences, National Academy of Sciences of the Republic of Armenia, Yerevan, Armenia
[j] Department of Cartography and Geomorphology, Yerevan State University, Yerevan, Armenia
[k] Human Origins Group, Faculty of Archaeology, University of Leiden, Leiden, the Netherlands

ARTICLE INFO

ABSTRACT

Barozh 12 is a Middle Paleolithic (MP) open-air site located near the Mt Arteni volcanic complex at the margins of the Ararat Depression, an intermontane basin that contains the Araxes River. Sedimentology, micromorphology, geochronology, biomarker evidence, together with an assessment of artifact taphonomy permits the modelling of site formation processes and paleoenvironment at a level of detail not previously achieved in this area. Obsidian MP artifacts were recovered in high densities at Barozh 12 from four stratigraphic units deposited during marine oxygen isotope stage 3 (MIS 3) (60.2 ± 5.7 −31.3 ± 3 ka). The MIS 3 sequence commences with low energy alluvial deposits that have been altered by incipient soil formation, while artifact assemblages in these strata were only minimally reworked. After a depositional hiatus, further low energy alluvial sedimentation and weak soil formation occurred, followed by higher energy colluvial (re)deposition and then deflation. Artifacts in these last stratigraphic units were more significantly reworked than those below. Analysis of plant leaf wax (n-alkane) bio-markers shows fluctuating humidity throughout the sequence. Collectively the evidence suggests that hunter-gatherers equipped with MP lithic technology repeatedly occupied this site during variable aridity regimes, demonstrating their successful adaptation to the changing environments of MIS 3.

1. Introduction

Marine oxygen isotope stage (MIS) 3 (~57−29 kya [Lisiecki and Raymo, 2005]) coincided with the Middle to Upper Paleolithic 'transition', a technological change that has often been associated with expansion of an anatomically modern human population into western Eurasia (e.g. Akazawa et al., 1998). However, the timing and directionality of human dispersals, population dynamics, and how these all relate to Paleolithic stone tool variability in southwest Asia remains poorly understood (Bar-Yosef and Belfer-Cohen, 2013; Dennell, 2008, 2017; Dennell and Petraglia, 2012; Groucutt et al., 2015; Bretzke and Conard, 2017). This uncertainty is due in part to a general scarcity of well-excavated and dated archaeological sites in most of the region for the relevant period and a sparse fossil record that often precludes the association of MP technologies with either Neanderthals or anatomically modern humans. Late

Pleistocene hominin population dynamics were likely influenced by numerous factors including regional topography, geological and hydrological dynamics, paleoenvironment, and the ability of hominins to maintain social networks and viable breeding populations (e.g. Dennell, 2017). In order to investigate the relative importance of these factors, chronologically controlled contextual data from archaeological sites in variable geomorphological settings are needed to document spatio-temporal patterns of hominin occupation and land use. Such was our aim in investigating the landscape surrounding the Mt Arteni volcanic complex in western Armenia.

Fieldwork in Armenia over the last twenty years has documented numerous cave/rock shelter and open-air sites that highlight the richness of the local MP record (e.g. Gasparyan et al., 2014). However, few MP open-air sites in Armenia have been excavated, and even fewer subjected to detailed geoarchaeological, geochronological, and paleoenvironmental analysis (Ghukasyan et al., 2011; Adler et al., 2014; Gasparyan et al., 2014; Egeland et al., 2016).

In this paper, we discuss the results of excavation, analysis of site formation processes, and the paleoenvironmental record at the site of Barozh 12. We describe and interpret the stratigraphy based on the results of geoarchaeological study, infrared stimulated luminescence (IRSL) dating, and biomarker analysis. We also examine artifact displacement and size sorting with reference to experimental and other empirical research on the effects of fluvial reworking of lithic artifact assemblages. Analyzing these data in conjunction with those obtained from laboratory sedimentological and micromorphological study, we assess the integrity of the lithic assemblages and their implications for hominin occupation at Barozh 12. Our aims are to: (1) Reconstruct the depositional, pedogenic, diagenetic, and erosional processes that contributed to the formation of the Barozh 12 archaeological site; (2) Determine the age of sediment deposition and the time range of site occupations; (3) Assess the degree to which artifact assemblages were affected by syn- and post-depositional processes; and (4) Evaluate the paleoenvironmental context of site occupations.

1.1. Regional setting and background

The Greater and Lesser Caucasus mountain ranges were formed by the Neogene collision of the Arabian and Eurasian plates (Philip et al., 1989). These processes also led to the development of the Armenian volcanic highlands, a physiographic area with steep elevation-dependent climatic and biotic gradients (e.g. Volodicheva, 2002). This area is rich in obsidian and other volcanic toolstone available in a variety of geomorphic contexts.

The site of Barozh 12 (40°20′01.26″N, 43°47′38.40″E; 1336 masl) is located ~5 km southwest of the town of Talin, and ~60 km west of Armenia's capital, Yerevan (Fig. 1). The site lies within the area of the Mt Arteni volcanic complex, that includes the Pokr (small) and Mets (big) Arteni volcanoes (1754 and 2047 masl, respectively). Today this area is characterized by steppic to semi-desert grassland, with some *Artemisia* species, and a semi-arid climate with average temperatures ranging from −5 °C − 30 °C annually, and an average of ~300−400 mL of precipitation per year (Volodicheva, 2002). The Mt Arteni volcanic complex comprises a series of volcanoclastic deposits, the most extensive of which is the 'Aragats flow' that trends in an E − W direction from Mets Arteni (Figs. 1 and 2). Obsidian-bearing perlitic lava flows and pyroclastic deposits have also been described within the volcanic complex (Karapetian et al., 2001). These comprise three geochemically distinct obsidian varieties, one associated with Mets Arteni, and two associated with Pokr Arteni (Frahm et al., 2014). Fission track and K−Ar dating of the obsidians associated with Pokr Arteni has yielded age estimates

Fig. 1. (A) Map of the study region showing locations of Middle Paleolithic sites and (B) geological map showing the Mt Arteni volcanic complex and location of Barozh 12.

Fig. 2. (A) Geological map of the Mt Arteni volcanic complex with location of Barozh 12. (B) Aerial photograph (Google Earth image 2020) of the Barozh 12 locality showing streams bordering the plateau and excavation area (red square). (For interpretation of the references to color in this figure legend, the reader is referred to the Web version of this article.)

of 1.45 ± 0.15 Ma and 1.26 ± 0.5 Ma respectively, while rhyolitic deposits associated with the edifice have been dated to 1.6 ± 0.15 Ma (Karapetian et al., 2001; Chernyshev et al., 2002; Lebedev et al., 2011, Fig. 2). The Mt Arteni volcanic complex itself is part of the much larger Aragats neovolcanic area (cf. Lebedev et al., 2011), which in addition to the Arteni vents, comprises two stratovolcanoes; Mt Aragats and Mt Arailer (4,090 masl and 2,614 masl respectively). Based on K−Ar dates from both vents and associated volcanic deposits, Mt Aragats had an eruptive history spanning 1.0−0.5 ma, while Mt Arailer erupted between 1.4 and 1.2 Ma (Chernyshev et al., 2002; Lebedev et al., 2011).

The Talin-Karmrashen plateau on which Barozh 12 lies is dissected by southward trending ephemeral streams, which are likely to have incised their beds during the Middle to Late Pleistocene as a response to tectonic uplift and base level change (Fig. 2A). South of the Barozh 12 plateau lies the NW margin of the Ararat Depression, an intermontane basin formed by subsidence induced by uplift along its margins and associated with faults running NW − SE (e.g. Lebedev et al., 2013; Avagyan et al., 2018). The basin separates the Aragats neovolcanic area from the Ararat Mountains in eastern Turkey and the Kars Plateau, and currently contains the floodplain of the Araxes River. Fine-grained sediments remaining

on the plateaus in the Barozh locality overlie spatially extensive ignimbrites associated with the Aragats Volcanic Province (AVP) which have been dated using a combination of K−Ar and ^{40}Ar/^{39}Ar in the Mt Aragats area to the interval 0.9−0.5 Ma (Mitchell and Westaway, 1999; Chernyshev et al., 2002; Aspinall et al., 2016; Gevorgyan et al., 2018).

The Mt Arteni volcanic complex itself has a long history of Paleolithic research (Panichkina, 1950; Sardaryan, 1954; Klein, 1966), however, the plateaus within a 1−4 km radius of the complex have only recently been investigated (Glauberman et al., 2016). Barozh 12 was discovered during survey in 2009. Obsidian MP artifacts were initially observed as a dense spread covering ~6000 m^2 area of the surface of a plateau 1−2 km southeast of the Mt Arteni volcanic complex. Preliminary excavation and archaeological and geological analysis were carried out at the northwestern part of the locality from 2014 to 2017 (Glauberman et al., 2016).

2. Materials and methods

2.1. Excavation and sampling

The topography of the Barozh 12 plateau was mapped at 5 m

intervals using a total station. Six 1 m x 1 m trenches were then excavated at 10−20 m intervals along two transects that bisect a slightly elevated area at the northeast end of the plateau (Fig. 3). The latter area had the highest surface artifact densities and was the location of a test trench excavated in 2009 (47A1; 0.5 × 0.5 m). One trench (49H1) was placed on the edge of a shallow gully ~ 35 m to the west of the main excavation area, where surface artifacts were rare to absent. Trenches were excavated down to the basal ignimbrite in arbitrary 10 cm spits within each lithostratigraphic unit, while the trenches ranged in depth from 0.4 m to 1.0 m. Artifacts were collected by spit and stratigraphic unit, while excavated sediments were dry screened through a 5 mm mesh, and all obsidian artifacts greater than 5 mm in maximal dimensions were retained.

The southern sections of all trenches were described and recorded according to standard protocols (Jones et al., 1999, Jerram and Petford, 2011), while Trench 36A7 was also sampled as continuous 2−5 cm-thick blocks for laboratory sedimentological and paleoenvironmental study (the locations of all samples taken from Trench 36A7 and described here are shown in Fig. 4). Trench 49H1 was also sampled for sedimentological analysis in the same manner as for Trench 36A7. Monolith samples measuring 15 × 8 cm were collected in stainless steel tins for micromorphological analysis across lithostratigraphic boundaries from Trench 36A7, while three sets of paired samples were taken for IRSL dating from the same trench. Bulk sediment samples (~150 g) were also collected in 5 cm intervals from Trench 36A7, from the surface to the basal ignimbrite, for extraction and quantification of n-alkanes (Fig. 4).

2.2. Laboratory methods

2.2.1. Sedimentological, geochemical and micromorphological analyses

Prior to laboratory sedimentological and geochemical analyses, the sediment samples from Trenches 36A7 and 49H1 were oven dried at 40 °C and then disaggregated with a pestle and mortar. The dried samples were passed through a 2 mm mesh, the weight of the >2 mm fraction recorded, and sub-samples of the <2 mm fraction were retained for bulk sedimentological and geochemical analyses. A further sub-sample of the < 2 mm fraction was passed through a 250 μm mesh and used for magnetic susceptibility measurements.

Mass specific magnetic susceptibility was measured on both <2 mm and <250 μm size fractions at low frequency (0.46 kHz, χ^{lf}) and high frequency (4.6 kHz, χ^{hf}) using a Bartington MS2 meter with an MS2C dual frequency sensor and following the protocol outlined in Dearing (1999). Values in Fig. 6 are expressed as SI units x10^{-6} m^3 kg^{-1}. Percentage frequency-dependent magnetic susceptibility ($\chi^{fd\%}$) was calculated as: $\chi^{fd\%} = 100 \times [(\chi^{lf} - \chi^{hf})/\chi^{lf}]$. Percentage carbonate content (%CaCO$_3$) was estimated from loss-on-ignition at 1000 °C following the method described by Heiri et al. (2001).

Grain size analysis was undertaken using a Malvern Mastersizer 3000 laser granulometer with a Hydro UM accessory. Prior to measurement, calcium carbonate and organic matter were removed with the successive addition of 10% hydrochloric acid and 10% hydrogen peroxide. Samples were then immersed in 0.5% sodium hexametaphosphate for 24 h to prevent coagulation. Prior to
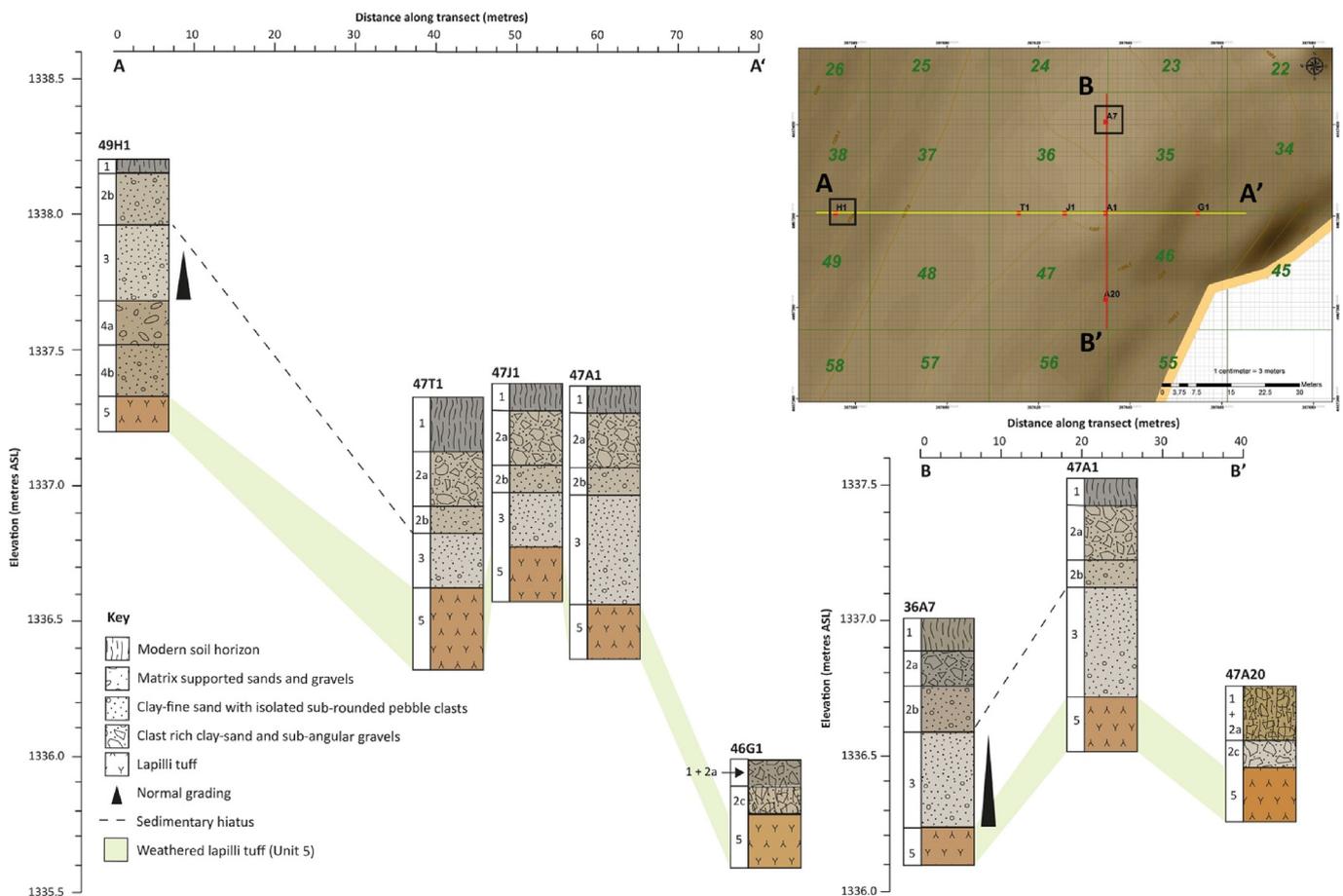
Fig. 3. Schematic stratigraphic cross section across the Barozh 12 excavated areas.
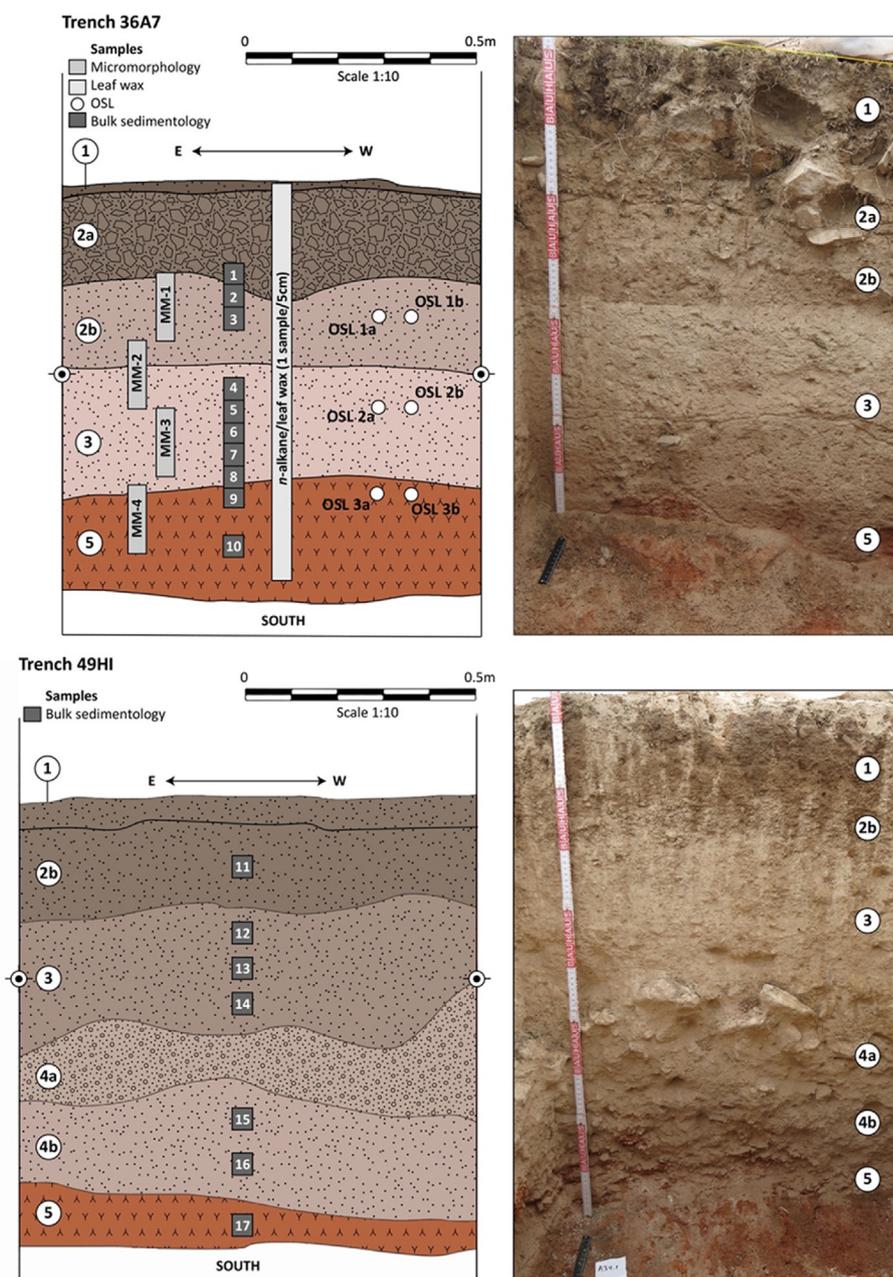
Fig. 4. Schematic stratigraphy and photos of sections of Trenches 36A7 (left) with sample locations and 49H1 (right). See Fig. 3 for trench locations.

measurement, samples were subject to ultrasound for 1 min. Each sample was measured 10 times using the Mie optical model in 116 channels ranging from 0.04 μm to 2000 μm (16 to −1 φ). Summary statistics for grain size data were calculated using the Folk and Ward (1957) method and employing the GRADISTAT statistical package (Blott and Pye, 2001).

Thin section samples for micromorphological analysis were prepared following the standard methodology employed by Quality Thin Sections Inc. (Arizona, USA). Once produced, thin sections were divided into 4 cm intervals, accounting for stratigraphic boundaries, and then studied using an Olympus BH-2 microscope at magnification x10 to x100 under transmitted plain-polarised, cross-polarised and oblique incident light. The strata observed in thin section were described and quantified according to the Bullock et al. (1985) criteria.

Elemental concentrations of bulk (<2 mm) sediment samples were measured using a Thermo Scientific Niton XL3 portable x-ray fluorescence analyzer (pXRF). Prior to measurement samples were homogenised and pressed into 10 cm^3 plastic pots and then covered with 6 μm Mylar® film. Samples were analyzed in a Niton FXL desk-top unit in 'Mining Cu/Zn' mode for 150 s (60, 30, 30 and 30 s on 'main', 'high', 'low' and 'light', respectively) using a 3 mm beam, with measurements repeated two times for each sample. Prior to each sample run, five standard reference materials (SRM) - NIST2709a, TILL4, RCRA; AL6061; SiO_2 blank - were analyzed. All data presented here are expressed as corrected ppm, based on linear regression analysis of pXRF measured values of each element against published SRM values. Specific elemental ratios (Zr/Rb, Ti/Al, Ba/Sr, K/Ti, Si/Al) were calculated using PAST paleontological statistics software (Hammer et al., 2001). The selected ratios were

used as they give an indication of particle size distribution and geochemical weathering within the Barozh 12 sequences (Sheldon and Tabor, 2009).

2.2.2. IRSL dating

Sediment samples were collected from Units 5, 3, and 2b using opaque stainless-steel tubes which were hammered horizontally into cleaned stratigraphic sections and wrapped in black plastic after removal. Potassium-rich feldspar (K-feldspar) grains were extracted from the sediment samples for optical dating and prepared for aliquot measurements to provide age estimates. We applied a single-aliquot post-IR IRSL (pIRIR) procedure (Thomsen et al., 2008) to determine equivalent dose (D_e) for our samples. Environmental dose rates were calculated respectively using sediment from within a ~30 cm radius from the sample tubes and material from within the sample tubes for gamma and beta dose rate, respectively. For further details on dose rate measurement, equivalent dose estimation, and age estimates, see Appendix A.

2.2.3. Plant leaf waxes (n-alkanes)

After collection, bulk sediment samples were kept frozen to avoid any post-collection alteration of the n-alkanes present in the samples (Brittingham et al., 2017). Sediment samples were placed in a Soxhlet extractor with 400 mL of 2:1 (v/v) dichloromethane:methanol and extracted for 48 h. Total lipid extract was evaporated under a gentle stream of N_2 gas at 40 °C before undergoing silica gel column chromatography. We eluted the aliphatic fraction with 2 mL hexane, the aromatic fraction with 4 mL dichloromethane, and the polar fraction with 4 mL methanol. When n-alkenes were identified as co-eluting in samples, neutral fractions were passed through a silver nitrate column to remove them. In samples with a high unresolved complex matrix, urea adduction was used to remove branched- and cyclic-alkanes.

We quantified n-alkanes on a Thermo-Scientific Trace Gas Chromatograph (GC) Ultra with a split/splitless injector and flame ionization detector (FID). Samples were separated on a BP-5 column (30 m × 0.25 mm x 0.25 μm) with helium as the carrier gas (1.5 mL/min). Oven temperature was set at 50 °C for 1 min, ramped to 180 °C at 12 °C/min, then ramped to 320 °C at 6 °C/min and held for 4 min. n-alkane standards of known concentration were run between every eight samples to ensure reproducibility and quantify unknown archaeological n-alkane concentrations.

2.2.4. Artifact analysis

To investigate site formation through the study of artifacts (cf. Schiffer, 1983; Nash and Petraglia, 1987; Bordes, 2003; Eren et al., 2011), we analyzed lithic artifact assemblages recovered from excavation trenches 36A7, 47J1, and 47T1 (n = 12,456). These trenches cut through virtually identical stratigraphy and contained the complete stratigraphic sequence. Aside from counts, the relatively few artifacts from Trench 49H1 (n = 147) are not included in this analysis. Artifacts were studied in two stages because they were often coated in carbonates. First an inventory was made, and then a detailed attribute analysis was carried out. Inventory included counting and categorizing all artifacts that could be identified to class (core, blank, flake < 2 cm, angular debris, angular debris <2 cm; Table 5 in Results) and determining completeness (broken, complete). The maximal dimensions of all artifacts were measured using calipers. Following Schick (1986, 1987) and Bertran et al. (2012), complete and broken artifacts are included in size distribution data.

After inventory production, but prior to attribute analysis, subsamples of artifacts with carbonate coatings from each stratigraphic unit were analyzed. The presence or absence of carbonate crusts, and if they covered one or all artifact surfaces were recorded.

If present, the percentage of crust coverage was recorded for the dominant surface. Coatings were then chemically removed from samples of artifacts from each stratigraphic unit (see Appendix A). Samples taken for cleaning and attribute analysis (total n = 950) attempted to include representative numbers of technologically diagnostic artifacts of all classes. The attribute analysis comprised the collection of detailed data on artifact manufacture techniques and typology (results forthcoming in a separate study). This analysis also included documentation of damage and weathering. It was observed whether artifacts displayed post-manufacture damage on their edges, indicated by non-anthropogenic flaking, rounding, and crushing. Damage was recorded on a scale from undamaged to severely damaged. Artifact weathering was recorded on a scale from un-weathered to severely weathered based on visual appearance of the intensity of hydration, or weathering rind development on artifact surfaces. This study includes the analysis of inventory data, complemented by data on artifact damage and weathering gathered during attribute analysis.

3. Results

3.1. Stratigraphy and sedimentology

As documented in Fig. 3, there is little stratigraphic variation between the test trenches, and the five principal stratigraphic units are identifiable across the whole excavated area, albeit that they are best represented in trenches 36A7 and 49H1 (Table 1).

The lowermost Unit (Unit 5) comprises medium to coarse sand with coarse ash to fine lapilli of predominantly rounded and Fe/Mn stained pumice. This unit outcrops at the base of all the test trenches and is the upper weathered surface of the Aragats ignimbrite deposits. In Trench 49H1, Unit 5 is overlain by Unit 4, which comprises interbedded matrix-supported (Unit 4a) and clast-rich (Unit 4b) sub-rounded to rounded pebbles and cobbles of pumice, felsic lava, and obsidian in a matrix of fine-medium sand. Unit 3 is present in Trenches 47T1, 47J1, 47AI and 36A7, and in 49H1 where it overlies Unit 4, and tapers downslope towards the SE of the excavation area. Unit 3 comprises normally-bedded fine sand-silty clay with isolated pebble-sized clasts of obsidian and pumice, while carbonate rhizoliths, powdery carbonate and gypsum intercalations are present throughout. There is a sharp contact between Unit 3 and the overlying Unit 2, and the latter comprises three subunits. Unit 2c is formed of clast-rich angular to sub-angular pebble−cobble sized gravels and is only found in Trenches 47A20 and 46GI, where it directly overlies Unit 5. Elsewhere, Unit 2 is represented by Units 2b and 2a. Unit 2b is a massive silt−medium sand with isolated rounded pebble sized clasts of ignimbrite. The matrix is formed of moderately-developed sub-angular, blocky peds, while rhizoliths are present throughout. Similar morphological properties are observable in Unit 2a, however, the latter is differentiated from Unit 2b by an increase in the size and frequency of gravel-sized clasts. The uppermost Unit (Unit 1) in the Barozh 12 sequence is a massive humic silt−fine sand with isolated pebble to boulder-sized clasts, representing the current surface soil. Hereafter the uppermost units are treated together as Unit 1+2a.

The results of sedimentological analysis of Barozh 12 indicate the deposits are poorly sorted (σ_ϕ= 1.7−2.5) and principally of a coarse silt − very fine sand texture (M_ϕ= 3.2−6.7), with a symmetrical−fine skewed distribution (Table 2). Broadly, the sequence is characterized by high χ^{lf} (24.6−109.5 SI Units) and relatively low %$CaCO_3$ (0.5−15.9%) values. In both the Trench 36A7 and 49H1 sequences, χ^{lf} of the <250 μm fraction is generally lower than those of the < 2 mm fraction, while $\chi^{fd\%}$ is relatively high in

Table 1
Sediment descriptions of Trenches 36A7 (A) and 49H1 (B).

Unit	Depth (meters below land surface)	Description	Interpretation
A Trench 36A7			
1	0.00–0.05	10 YR 4/3 dark greyish brown (10 YR 4/2 moist) humic silt-fine sand with moderate medium sand to granular, and occasional pebble–boulder-sized, sub-rounded tuff clasts. Matrix formed of fine pebble-sized blocky aggregates. Frequent fine and moderate medium roots. Poorly sorted. Diffuse boundary to:	Modern humic A horizon
2a	0.05–0.20	10 YR 4/3 dark greyish brown (10 YR 4/2 moist) humic silt–fine sand with moderate medium sand to granular and occasional pebble boulder-sized, sub-rounded tuff clasts. Matrix formed of fine pebble-sized blocky aggregates. Frequent fine and moderate medium roots. Poorly sorted. Diffuse boundary to:	Pedogenically modified (B horizon) colluvial sediments
2b	0.20–0.40	7.5 YR 7/2 pinkish white, (5 R 5/3 moist) brown silt to fine sand with moderate medium sand to fine pebble-sized sub-angular carbonate-coated tuff and obsidian clasts. Rarer non-carbonate coated tuff pebbles. Carbonate bonded throughout. Rare fine roots. Well sorted. Diffuse boundary to:	Pedogenically modified (B horizon) fine-grained alluvial sediments
3	0.40–0.70	7.5 YR 7/2 pinkish white (5 YR 5/4 moist), clay to fine sand. Frequent sub-angular to fine pebble sized tuff clasts decreasing upward to rare at top (fining up sequence). Rare sub-angular pebble-sized obsidian clasts. Carbonate bonded throughout. Moderately sorted. Sharp boundary to:	Pedogenically modified (B horizon) fine-grained alluvial sediments
5	0.70–0.90	2.5 YR 5/6 red, (2.5 YR 5/6 moist) medium to coarse sand. Well sorted.	Weathered ignimbrite (C horizon)
B Trench 49H1			
1	1.0–0.05	10 YR 5/2 greyish brown (10 YR 5/3 moist) humic silt to medium sand with moderate sub-rounded carbonate-coated granular to pebble-sized tuff, and rare cobble-sized sub-rounded carbonate coated tuff clasts. Frequent fine roots. Matrix formed of granular-sized aggregates. Moderately sorted. Diffuse boundary to:	Modern humic A horizon
2	0.05–0.25	10 YR/6/3 pale brown (7.5 YR 5/3 moist) clay to medium sand with frequent sub-rounded and sub-angular carbonate- and clay-coated granular sized aggregates, these orientated parallel to the bedding place. Occasional sub-rounded carbonate-coated coarse pebbles. Moderate-fine roots. Moderately sorted. Sharp boundary to:	Pedogenically modified (B horizon) fine-grained alluvial sediments
3	0.25–0.50	10 YR 7/3 very pale brown (7.5 YR 5/4 moist) silt–clay fining upwards from medium sand at base. Moderate granular- to medium pebble-sized tuff and obsidian clasts, decreasing in frequency upwards through the stratum. Gravel-sized particles are randomly orientated. Moderately sorted. Diffuse boundary to:	Pedogenically modified (B horizon) fine-grained alluvial sediments
4a	0.50–0.70	10 YR 7/3 pink (7.5 YR/5/4 moist) matrix-supported gravel of sub-rounded carbonate-coated pebbles and cobbles of tuff, perlite and obsidian in a fine sand matrix. Gravel particles mostly lie parallel to bedding plain, but a small proportion are perpendicular. Poorly sorted. Diffuse boundary to:	Primary channel or channel lag deposit (B horizon)
4b	0.70–0.85	7.5 YR 7/3 pink (7.5 YR 5/4 moist) fine to medium cobbles and with frequent sub-angular to sub-rounded pebble-sized clasts of tuff, obsidian and perlite. Sharp boundary to:	Primary channel or channel lag deposit (C horizon)
5	0.85–1.0	2.5 YR 5/6 red (2.5 YR 5/6 moist) medium to coarse sand with frequent darker coarse sand particles. Well sorted.	Weathered tuff (C horizon)

Table 2
Grain size statistics for Barozh 12. Shown are grain size parameters (φ) and % contribution of sand, silt and clay. Grain size parameters calculated following methodology of Folk and Ward (1957).

Sample Code	Unit	Grain size parameters (φ)					% SAND	% SILT	% CLAY
		Mean	Sorting	Skewness	Kurtosis	Median grain size (D_{50})			
Trench 36A7									
BAR12-1	2b	4.738	2.491	0.156	0.884	4.445	43.1%	52.2%	4.7%
BAR12-2	2b	4.739	2.543	0.128	0.979	4.442	42.7%	52.5%	4.8%
BAR12-3	2b	4.578	2.389	0.161	0.968	4.284	45.1%	51.2%	3.7%
BAR12-4	3a	4.190	2.288	0.160	1.018	3.957	50.8%	46.8%	2.4%
BAR12-5	3a	3.882	2.166	0.167	1.042	3.682	56.2%	42.4%	1.4%
BAR12-6	3a	4.161	2.066	0.161	1.051	3.932	51.4%	47.5%	1.1%
BAR12-7	3a	3.744	2.414	0.064	1.050	3.662	56.0%	42.7%	1.3%
BAR12-8	3a	4.030	2.145	0.134	1.069	3.845	53.1%	45.7%	1.3%
BAR12-9	3a	3.871	2.045	0.141	1.086	3.708	56.0%	43.0%	1.0%
BAR12-10	5	3.250	1.715	−0.069	1.140	3.313	67.5%	32.5%	0.0%
Trench 49H1									
BAR12-11	2	6.682	2.464	−0.017	1.049	6.839	14.0%	70.0%	16.0%
BAR12-12	3a	6.097	2.434	−0.024	0.896	6.257	21.6%	68.3%	10.2%
BAR12-13	3a	5.572	2.648	0.163	0.925	5.349	30.3%	59.6%	10.1%
BAR12-14	3a	5.287	2.074	0.141	1.042	5.140	26.9%	67.5%	5.6%
BAR12-15	4b	4.594	2.549	0.047	0.964	4.511	41.9%	53.9%	4.2%
BAR12-16	4b	4.715	2.384	0.089	0.966	4.565	40.4%	55.6%	4.0%
BAR12-17	5	3.262	2.344	0.035	0.957	3.303	62.4%	36.7%	0.9%

both the <2 mm and <250 μm fractions (6.1−14.4%).

In both Trenches 36A7 and 49H1 there are variations in the sedimentological parameters between strata (Fig. 5). In Trench 36A7, Unit 5 is characterized by elevated χ^{lf} and low $CaCO_3$ contents, and has a fine sand texture. Clay content increases in the overlying Unit 3, and as a result a lower median particle size was observed than in Unit 5. This change coincides with a decrease in χ^{lf}, and an increase in %$CaCO_3$. Unit 2b is characterized by a further increase in clay content, and elevated values of $CaCO_3$ and χ^{lf} in comparison to Unit 3. The particle size distribution of strata in Trench 49H1 (Fig. 6 and Table 2) is generally finer than in comparable units in Trench 36A7, and the sediments are predominantly silty in texture. In Trench 49H1, Unit 5 is characterized by high χ^{lf} and a poorly sorted fine-sand dominated grain size. The overlying Unit 4b exhibits a coarse silt texture; lower χ^{lf}, and higher %$CaCO_3$ than in Unit 5. Unit 3 is characterized by low χ^{lf} and higher $CaCO_3$ content compared to the lower Units, while there is also an increase in clay content from 15 to 25% upwards through the unit. High clay and $CaCO_3$ content, and low χ^{lf} characterize Unit 2b. In both the Trench 36A7 and 49H1 sequences, $\chi^{fd\%}$ exhibits a trend to lower values towards the top of the sequence.

3.2. Thin section micromorphology

The main micromorphological properties of Trench 36A7 (upper part of Unit 5, Unit 3, Unit 2b) are presented in Table 3. The overall microstructure of the sequence ranges from massive to granular with porosity ranging from simple vughs and channels at the base to intergranular towards the top of the sequence. The coarse-fine (c/f at 20 μm) related distribution is closed−open polyphric throughout with a ratio of 2:3 to 1:1, with the main constituents of the coarse mineral grains being typic and banded pumice and scoria, mafic and felsic lava fragments, obsidian fragments and large (up to 100 μm, α-axis length) single feldspar (mainly plagioclase) grains. Also present throughout the sequence are rounded aggregates of clay and calcite, rare fragments of micritc-microspartic carbonate and clay and micritic calcite rich sand. The fine fraction (<20 μm) is predominantly silt-sized with volcanic glass, microspartic calcite and gypsum as the primary constituents, while the b-fabric is undifferentiated to crystallic throughout. The whole sequence is characterized by a range of textural, crystalline and fabric pedofeatures and compound pedofeatures; these take form as primarily infillings, coating and hypocoatings, with rarer occurrences of nodules.

Variation in the type and frequency of pedofeature distribution is observed through the Trench 36A7 sequence. Unit 5 is characterized by an approximately equal abundance of calcitic and gypsic pedofeatures. These frequently take the form of dense complete-incomplete infillings of voids with microspartic subhedral equant calcite crystals or of lenticular-tabular microcrystalline gypsum crystals (Fig. 7A). Coatings and hypocoatings of grains by microcrystalline gypsum or microspartic calcite are also common. Pumice grains frequently exhibit peculiar-dotted weak-moderate alteration into microspartic calcite. Also associated with this unit are rare occurrences of clay silt and calcite grain capping, and pendent cements.

Unit 3 is characterized by an increase in abundance of gypsic pedofeatures through the unit. These features take form as intercalations of tabular and lenticular gypsum crystals in the groundmass, and dense, continuous infillings of voids, forming a vermiform structure. Also present are common occurrences of gypsic pendant cements and grain coatings (Fig. 7C); frequently these are found in association with calcite pendant cements and impure calcite-clay coatings, forming compound pedofeatures (Fig. 7B). Through Unit 3, the frequency of gypsum in the

groundmass increases, allied to a general decrease in crystal size (with microcrystalline gypsum becoming more frequent), and the appearance of rare typic gypsum nodules. Calcitic and textural pedofeatures are also present through Unit 3. These take form as very rare occurrence of calcified root tissue and rare occurrences of discontinuous microspartic void infillings. Large clasts within this unit are commonly characterized by layered coatings. This is evident in Fig. 7D, in which a compound coating comprising multiple convolute lamina of micritic calcite and impure clay overlain by a layer of clay with sand size (volcanic glass and feldspar grains) particles, dusty clay micritic calcite lamina, and a hypocoating of microcrystalline and crystalline gypsum.

The contact between Unit 3 and Unit 2b (MM2a) is characterized by an abrupt convolute-broken boundary (Fig. 7E). Associated with the boundary are sub-vertical passage features in Unit 3, and rare intraclasts comprising material from Unit 3 in the lower parts of Unit 2b. Associated with the contact in Unit 2b is an increase in frequency of sand-size pumice and rhyolite fragments, frequently with peculiar-dotted alteration into calcite. Unit 2b is characterized by the absence of gypsic pedofeatures and crystal intergrowths in the groundmass (Fig. 7H). Calcitic crystalline pedofeatures are common and comprise microspartic-micritic calcite and clay and weakly impregnative micritic calcite hypocoatings around grains and obsidian fragments (Fig. 7G). At the base of the unit, redoximorphic features are present. These take form as rare discontinuous void coatings or spherule-shaped Fe/Mn accumulations (Fig. 7F), and rare compound aggregate and compound impregnative typic nodules of Fe/Mn. In the upper part of Unit 2b these redoximorphic features are absent.

3.3. Sediment geochemistry

Elemental concentrations of selected major and minor elements (Al, Si, P, S, K, Ca, Ti, Fe, Zn, Rb, Sr, Zr and Ba) for Trench 36A7 and 49H1 are presented in Fig. 8. A principal component analysis (PCA) was undertaken using normalized (log-transformed) concentrations of the selected elements to identify and characterize differences between stratigraphic units (Fig. 9A). Results of this analysis reveal that the first two principal components account for 80.56% of the variance in the dataset (PC1 = 59.67%, PC2 = 20.83%). While high Ca values contribute to negative loadings on PC1, elevated values of Ti contribute to positive loadings. In contrast, positive loadings of PC2 are controlled by elevated values of Ca, Zn, Fe and Al, whereas negative loadings are influenced by high values of Sr and Zr. Evident in the PCA is differential clustering of units based on their elemental composition with Units 5 and 3 having differences in bulk chemical composition compared to the rest of the Barozh 12 strata. The spread of data points associated with Unit 3 observable in the PCA is the function of marked shifts in the major and minor elemental concentrations through this unit, with decreases upwards in the observed concentrations of Si, P, K, Ti, Fe, Rb and Zr.

Elemental ratios of Zr/Rb, Ti/Al, K/Ti, Ba/Sr and Si/Al are plotted against depth in Fig. 9B and although there is considerable variability, three broad trends can be identified. First, Zb/Rb ratios vary throughout both Trench 36A7 and 49H1 sequences in concordance with particle size (Zr/Rb – d50 $r^2 = 0.64$ [n = 17]), i.e. high Zr/Rb ratios are found in association with a coarser particle size distribution. Second, decreases in three of the elemental ratios (Ti/Al, Ba/Sr and Si/Al) are observable upwards through Unit 3. Conversely, K/Ti ratios show an increase through this Unit. Third, there are spatial differences in elemental ratios within the same Unit. This is most apparent in Unit 3, where the decreasing trends in three element ratios (Si/Al, Ti/Al and Ba/Sr) observable in Trench 36A7 are not apparent in 49H1.
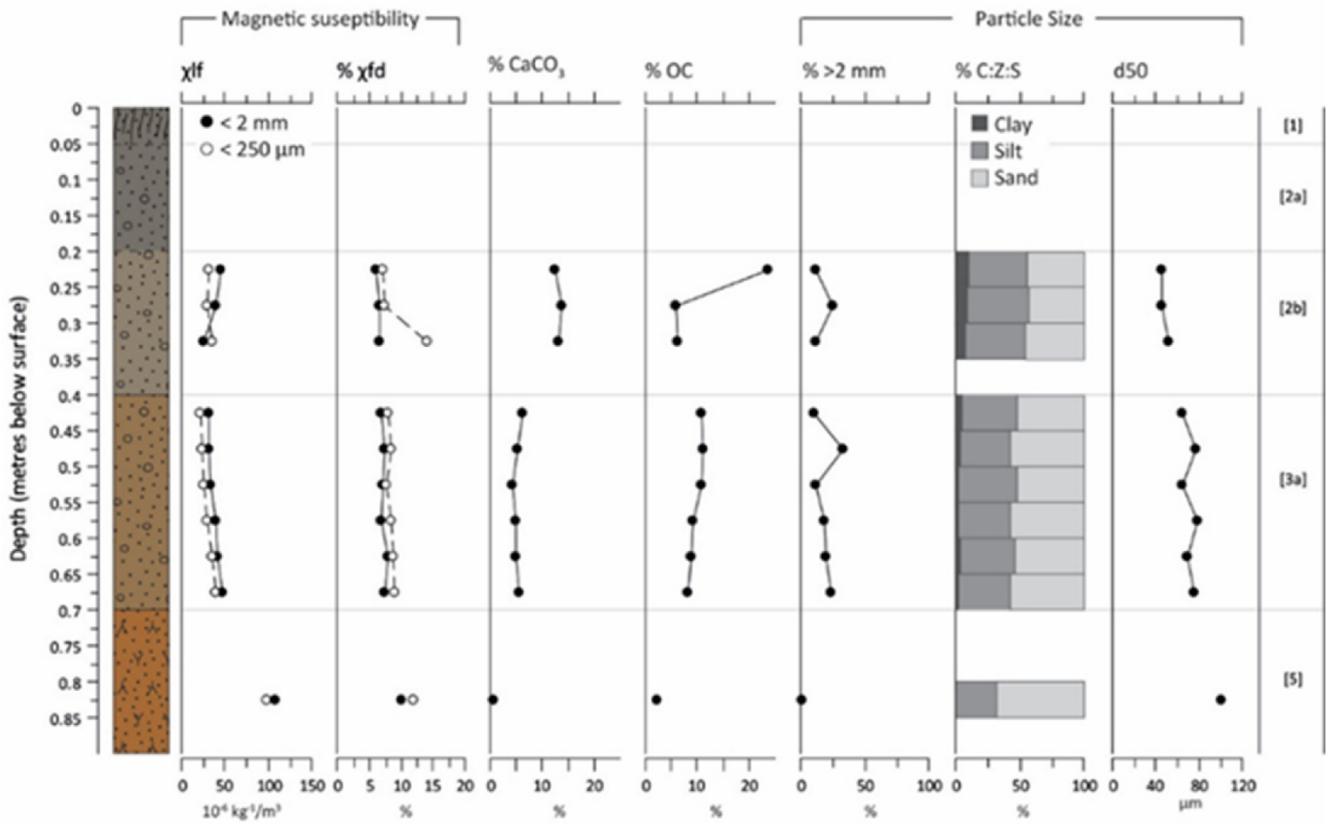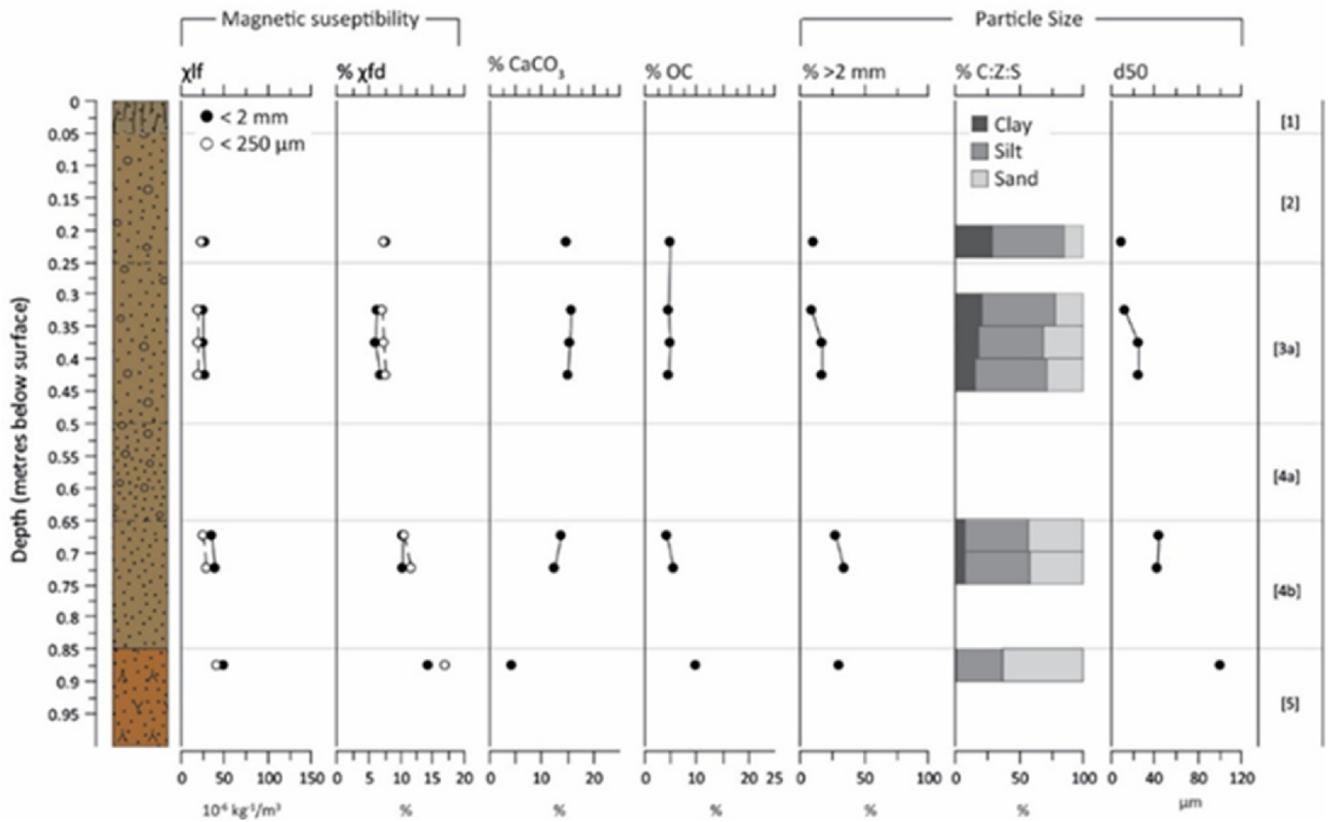
Fig. 5. Results of sedimentological analysis in Trench 36A7 (A) and Trench 49H1 (B).
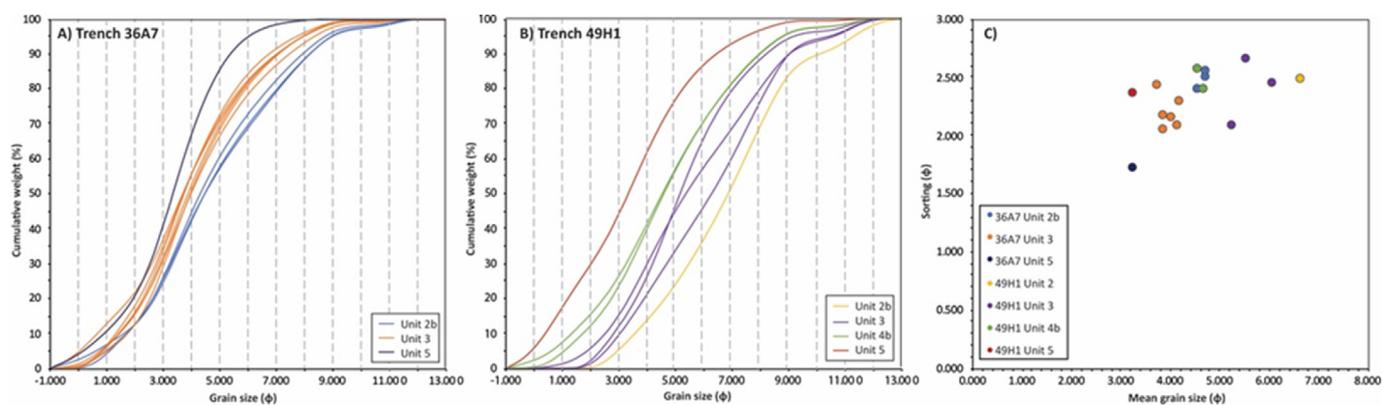
Fig. 6. Grain size distribution of the Barozh 12 sequence. (A) and (B) Cumulative frequency plots showing grain size distribution from Trenches 36A7 and 49H1 respectively. (C) XY plot comparing mean grain size to sorting (calculated following equation of Folk and Ward (1957)) of grain size samples from the Barozh 12 sequence.

3.4. Sedimentological interpretation

The elevated χ^{lf} and coarse, poorly sorted particle size distribution of Unit 5 is consistent with ignimbrite, while the presence of calcium carbonate supports the field observations of *in situ* weathering that is in part caused by incipient pedogenesis prior to the deposition of the overlying stratigraphic units.

The sedimentological properties of Units 4–2 are consistent with alluvial sedimentation. Such an interpretation is suggested by the grain size distribution of the strata, which show generally poorly sorted textures (Fig. 6) and the presence of isolated sub-rounded to sub-angular granule—pebble sized clasts within Units 4b, 3 and 2b. Clasts with a similar morphology and size also comprise Unit 4a, indicating this stratum was deposited by moderate energy alluvial processes. An alluvial genesis is also indicated by the presence of diverse volcanogenic lithologies, suggesting the transport of material from outside of the Barozh 12 locale. The presence of perlite and obsidian clasts indicates erosion of material likely occurred in the area north of Barozh 12, where these deposits outcrop locally and were subsequently transported to the site (Fig. 2A).

The sedimentological properties of Unit 3 and Unit 2b are consistent with low energy alluvial sedimentation. Increasing carbonate and clay content upward through both of these units indicates these strata were subject to pedogenesis, resulting in carbonate enrichment and clay illuviation. It is important to note, however, that there is a sharp boundary between Unit 3 and Unit 2b, indicating a likely break in sedimentation between the two overbank phases and probably also, truncation of the lower unit. Unit 4a, which only occurs as a localized stratum within Trench 49H1, is interpreted as a primary channel, or the lag of a channel deposit, and Unit 4b to represent lower energy alluvial sedimentation. The formation of Unit 2a is attributed to colluvial processes while Unit 1 is the present-day soil which has developed within the colluvium of Unit 2a.

It is most probable that local and regional volcanic lithologies provide the ultimate source of the majority of particles forming the alluvial sediments. This is suggested by the high X^{lf} values observable throughout the sequence, these reflecting inputs of ferrimagnetic minerals and grains derived from igneous sources (Dearing, 1999). Decreases in X^{lf} upward through both sequences are concomitant with increase in $CaCO_3$, reflecting the diamagnetic nature of the latter constituent (Dearing, 1999), rather than a shift in sediment supply. Such an interpretation is supported by the relatively constant Ti concentration observable through the sequences in both Trench 36A7 and 49H1. As Ti concentration is

highly variable in different igneous rock types (Sayyed and Hundekari, 2006), the consistent values observed in the Barozh 12 sequence likely reflect unchanging parent material (i.e. alluvial reworking of principally locally-derived material was occurring, rather than the incorporation of far-traveled material from other igneous sources). The high $\%\chi^{fd}$ values observed throughout the Barozh-12 sequence are also likely inherited from volcanic material rather than developing as a result of pedogenesis (c.f. Srivastava et al., 2012).

The micromorphological properties of Trench 36A7 are consistent with the inferred multiple phases of incipient soil formation within the fine-grained alluvium (Units 3 and 2b) and ignimbrite (Unit 5). Evidence for illuviated fine-grained material is evident throughout Units 2b, 3 and 5, and is also seen in the presence of impure calcite-rich clay coatings on grains and rounded aggregates. The occurrence of laminated coatings (Fig. 7) suggests that the illuviation process was active over several events (Kuhn, 2003), each related to distinct phases of pedogenesis. Silt—clay capping of grains observable in Units 3 and 5 is likely associated with the desiccation or freeze-thaw of the sediments and which resulted in the rapid physical translocation of coarse material from the upper part of the sediment sequence, and its accumulation in the lower part (Van Vliet-Lanoe et al., 2004). Weathering and thus pedogenesis is also suggested by the presence of clay-calcite aggregates and sedimentary lithic fragments throughout the sequence. Indeed, the presence of calcite pedofeatures throughout the Barozh-12 sequence suggests accumulation of calcium carbonate as a result of dissolution, transportation, and reprecipitation of calcite in semi-arid environmental conditions (Durand et al., 2010). Specifically, the presence of pendant cements and hypo-quasi calcite coatings indicate their formation in the vadose zone in association with percolation of water through the sequence (Durand et al., 2010). The abundance of gypsic features within Unit 3 is consistent with the evaporative concentration of Ca^{2+} and SO_4^{2}. The occurrence of these features in Unit 3 suggests a lowering of the water table and desiccation of sediments after deposition, with later formation of gypsum due to a fluctuating water table rich in Ca^{2+} and SO^{2-}_4. Moreover, the absence of rounded gypsum crystals in the groundmass in Unit 3, allied to the presence of gypsum infillings, pendant cements and nodules, strongly suggests *in situ* intrusive growth of gypsum, with the vermiform structure observable throughout Unit 3 indicative of progressive enrichment of gypsum in the phreatic zone over time (Toomanian et al., 2001). The increase in the abundance of microcrystalline gypsum towards the top of Unit 3 is likely related to an increased distance from the water table (Yamnova, 1990; Toomanian et al., 2003). Fluctuating water table

Table 3
Summary of the micromorphological features in Barozh 12 thin sections. C/F = coarse to fine ratio (20 μm), M = massive, s.a = slide area, Ch = channel, Vu = vughs, Un = Undifferentiated, C = crystallitic; Gr = granular; P = planar voids; IG; intergranular texture, – = not detected, * = rare (<0.5%), ** = rare (0.5–2%), *** = few (2–5%), **** = common (>5%).

Sample	Depth (below ground surface)	Unit	Microstructure	Voids %s.a	Voids Type	C/F ratio	B-fabric	Calcific Nodules	Calcific Coatings	Calcific Infillings	Gypsic Nodules	Gypsic Coatings	Gypsic Infillings	Textural Clay coatings	Textural Clay-silt caps	Fe–Mn concentration features	Organic Amorphous	Organic Plant residue	Passage features
1a	21–28.5	2b	M, IG	2–5	Ch, Vu	50:50	C	–	**	**	–	**	**	–	–	*	**	–	*
1b	28.5–36	2b	M, IG	2–5	Ch, Vu	60:40	C	–	**	**	–	**	**	–	–	*	**	–	*
2a (above contact)	34–36	2b	M	5	Ch, P	70; 30	C	–	**	–	–	–	–	*	–	**	**	–	–
2a (below contact)	36–41.1	3	M	5	Ch, Vu	30:70	C	*	–	–	**	***	***	–	–	–	*	–	**
2b	41.5–49	3	M	10	Vu, Ch	40:60	C	–	–	*	**	***	***	**	*	–	**	–	*
3a	48–55.5	3	M	10–15	Vu, Ch	40:60	C	–	*	*	*	***	***	**	*	–	*	*	–
3b	55.5–63	3	M	10–15	Vu	40:60	C	–	**	**	*	***	***	***	–	*	*	*	–
4a	632–69.5	3	M	15–30	Vu, Ch	50:50	C	–	**	**	–	***	**	–	–	–	**	–	–
4b	69.5–77	5	M	5	Vu, Ch	6040	Un	–	**	**	–	**	**	–	–	–	**	–	–

elevations during the period of gypsum formation in the Trench 36A7 sequence is evident through the presence of pendant cements, indicative of gypsum formation associated with the downward gravitational movement of water in the vadose zone, supported by the presence of weakly impregnative-type nodule formation, the latter frequently polyphasic in nature. The source of sulfur forming these features, however, is unlikely to be associated with the dissolution of calcium-sulphates in the local bedrock (Poch et al., 2010). The principal geological formations in the Barozh locality are felsic lavas and pyroclastic deposits, both of which have a low sulfur content (Gill, 2010). Thus, it is more probable sulfur has been derived from an extra-local source, likely by aeolian activity.

The redoximorphic features that characterize Unit 2a are associated with the segregation of iron-manganese oxides due to wetting and drying over numerous redox cycles (Lindbo et al., 2010). Furthermore, the presence of both impregnative and intrusive features is consistent with the accumulation of oxidized Fe and Mn. This is associated with a shift to aerobic conditions after a prolonged period of water saturation (Lindbo et al., 2010), an observation that is consistent with relatively high Fe concentrations observed in Unit 2a in comparison to the rest of the sequence.

Changes in the ratio of Zr/Rb, Ti/Al, Ba/Sr and Si/Al have previously been shown to reflect weathering processes (Ti/Al, Si/Al, and Ba/Sr), particle size shifts (Zr/Rb), and changes in source material in areas with volcanic parent material (Dypvik and Harris, 2001; Sheldon and Tabor, 2009). Hence the ratios can also be used to infer the intensity of weathering and pedogenesis through the Barozh 12 sequence (Fig. 9B). Decreases in Ti/Al, Si/Al and Ba/Sr ratios through Unit 3 are thus interpreted as reflecting enhanced weathering intensity upwards through the stratum. This would have acted to increase the accumulation of clay forming minerals (resulting in higher Al concentrations), and cause leaching of more soluble minerals through the sequence (as observable in the relatively lower Sr and Ba concentrations through Unit 3 [Sheldon, 2009]). Translocation of clay-forming minerals in Unit 3 is also indicated by decreasing concentrations of K and Fe upwards through the stratum (Sheldon and Tabor, 2009).

In summary, the sedimentary evidence from Barozh 12 indicates sediment accumulation in an alluvial setting and alternating between overbank sedimentation and deposition in a channel. Deposits forming by colluvial processes, albeit onto the floodplain, complete the depositional story. There are at least four phases of pedogenesis, the first within upper strata of the ignimbrite and occurring prior to alluvial deposition, the second associated with the deposition of Unit 3, the third during the deposition of Unit 2b and the last in the recent past. Micromorphological evidence suggests that there was an interval of water table reduction and aridity between the deposition of Unit 3 and Unit 2b and that this caused gypsic enrichment of Unit 3. The shift to slightly more humid and higher water table conditions may coincide with the deposition of the overlying alluvial stratum (Unit 2b).

3.5. IRSL chronology

The D_e values, dose rates and age estimates from IRSL dating are summarized in Table 4 (see also Appendix A). The age estimates for the two lower samples Barozh-OSL-3 from Unit 5 and Barozh-OSL-2 from Unit 3 are 50.7 ± 6.1 ka and 60.2 ± 5.7 respectively, and both are statistically consistent with each other at 2σ. The two components identified for the uppermost sample (Barozh-OSL-1 from Unit 2b) yielded ages of 31.3 ± 3.0 and 7.1 ± 1.3 ka, respectively. The presence of relatively young grains (dated to ~7 ka) in Barozh-OSL-1 might be caused by bioturbation including rooting as observed in Units 1, 2a, and 2b in the form of modern roots, root casts, and rhizoliths (Table 1). The age of the dominant component in Unit 2b
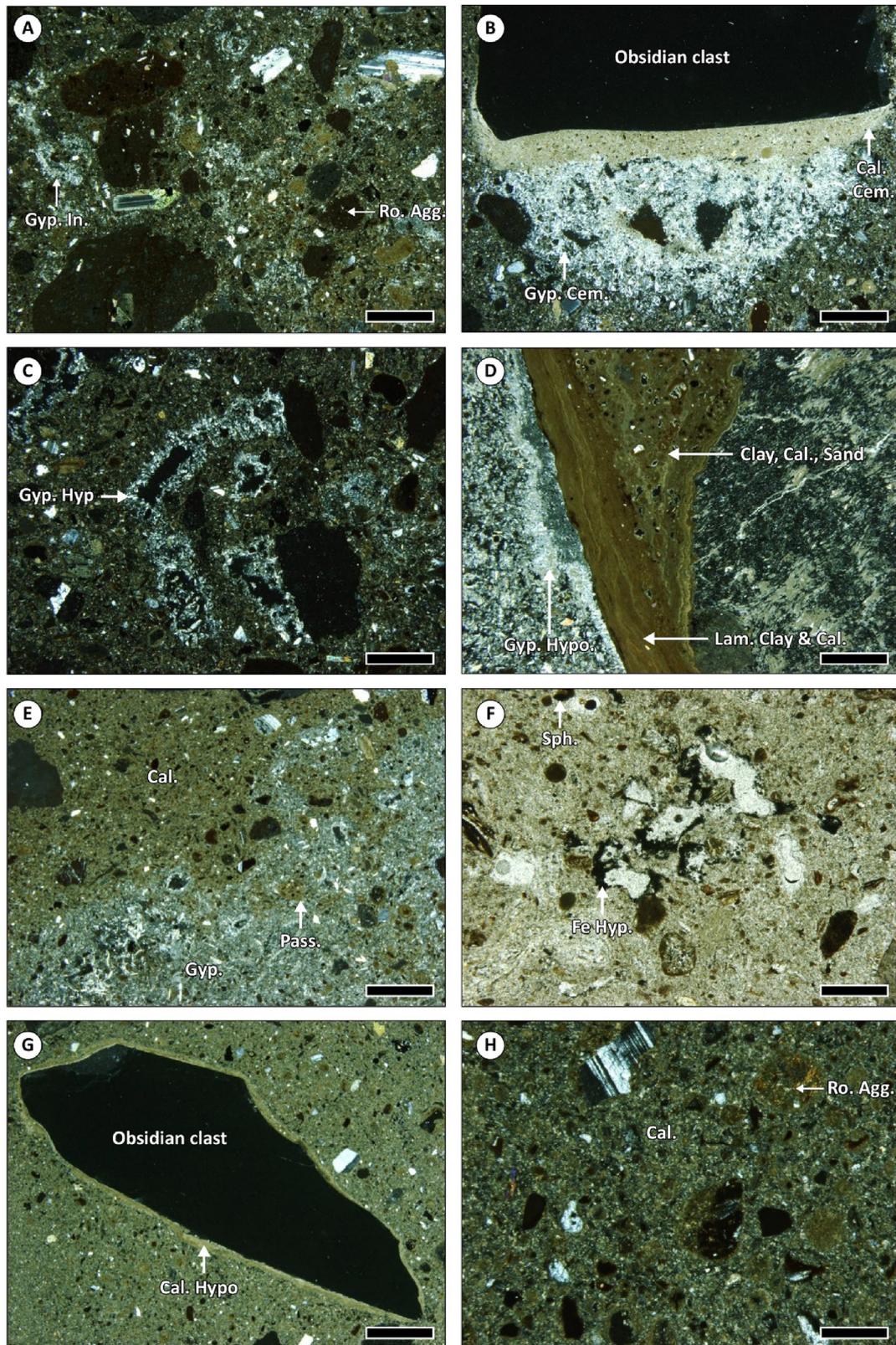
Fig. 7. Photomicrographs of key micromorphological features in the Barozh 12 sequence. Scale bar = 500 μm. A full description of the microfeatures is in the main text. A) Microstructure of Unit 5, showing presence of gypsum infillings of voids (Gyp. In.) and rounded clay aggregates (Ro. Agg.). B) Obsidian clast from Unit 3 with a compound pendant cement of calcite (Cal. Cem.) and gypsum (Gyp. Cem.). C) Microstructure of Unit 3 showing gypsum hypocoatings (Gyp. Hyp.) of voids. D) Compound coating of a clast in Unit 3. Coating comprise calcite with clay and sand grains (Clay, Cal., Sand), irregularly laminated clay-calcite (Lam. Clay & Cal.) and gypsum (Gyp. Hypo.). E) Contact between Unit 3 and 2b showing difference in calcitic groundmass (Cal.) that characterizes Unit 2b and the gypsic (Gyp.) groundmass that characterizes Unit 3. Also shown is a passage feature (Pass.) associated with the boundary. F) Fe/Mn hypocoatings (Fe Hyp.) and spherules (Sph.) in Unit 2b. G) Obsidian clast with a micrite-microspartic hypocoating (Cal. Hypo.) from Unit 2b. H) Microstructure of Unit 2b showing the micritic-microspartic groundmass (Cal.) and the presence of rounded clay aggregates (Ro. Agg.).
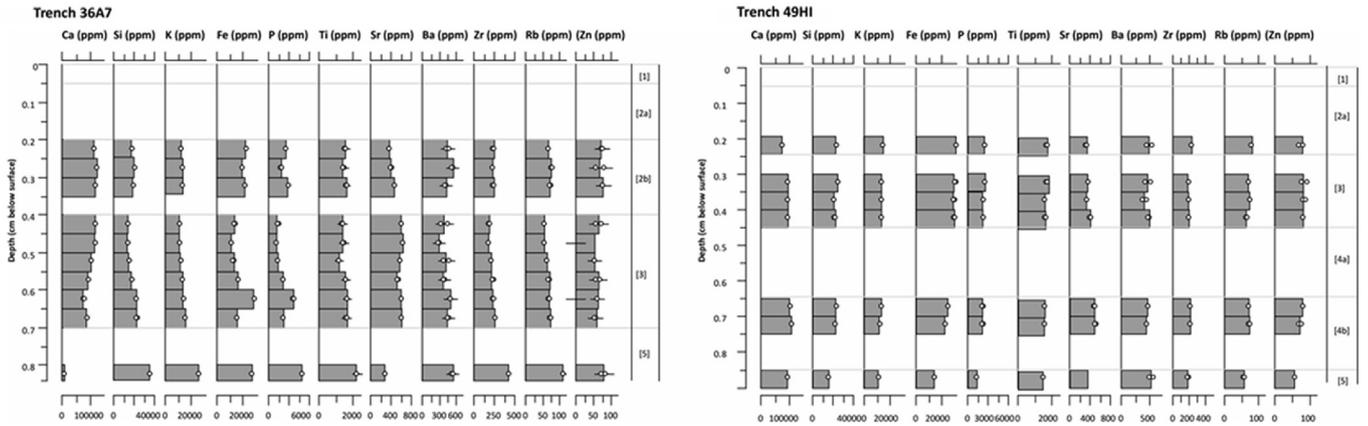
Fig. 8. Plotted elemental concentrations of selected elements from Trench 36A7 (left graph) and 49H1 (right graph). White circles indicate corrected concentrations (in ppm), black horizontal lines indicate 1 σ standard deviation measurement error. Grey bars indicate median values based on repeat measurement.
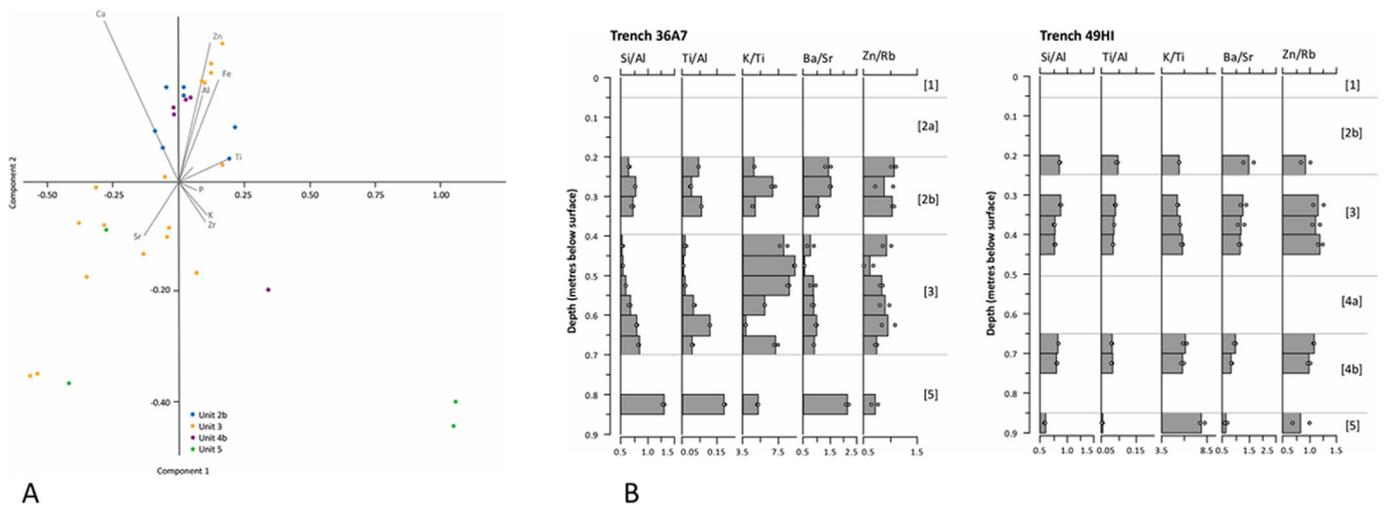
Fig. 9. (A) PCA of elemental concentrations (Al, Si, P, K, Ca, Ti, Fe, Zn, Rb, Sr, Zr, Ba) from the Barozh sequence. Data are normalized (log-transformed) and different units represented by different color circles, (B) ratios of selected elements (Si/Al, Ti/Al, K/Ti, Ba/Sr, Zn/Rb) from Trenches 36A7 and 49H1. (For interpretation of the references to color in this figure legend, the reader is referred to the Web version of this article.)

Table 4
Burial depths, units, grain sizes, dosimetry data, D_e and ages for the K-feldspar samples.

Sample	Depth(cm)	Grain size (μm)	Water Content (%)[a]	Gamma dose rate (Gy/ka)	Ext. beta dose rate (Gy/ka)	Int. beta dose rate (Gy/ka)	Cosmic ray (Gy/ka)	Total dose rate(Gy/ka)	Over-dispersion(%)	pIRIR,90 $D_e(Gy)$[b]	Age model	Age (kyr)[b]
Barozh-OSL-1	30	180–212	15 ± 5 (12)	0.89 ± 0.05	1.43 ± 0.08	0.74 ± 0.13	0.268	3.29 ± 0.16	64 ± 8	30 ± 3 (n = 10)	FMM-1(34%)	7.1 ± 1.3
										110 ± 8 (n = 20)	FMM-2 (66%)	31.3 ± 3.0
Barozh-OSL-2	50	90–125	15 ± 5 (13)	0.78 ± 0.05	1.21 ± 0.07	0.44 ± 0.08	0.265	2.65 ± 0.12	35 ± 6	166 ± 13 (n = 24)	CAM	60.2 ± 5.7
Barozh-OSL-3	70	90–125	15 ± 5 (14)	0.88 ± 0.05	1.39 ± 0.07	0.44 ± 0.08	0.261	2.92 ± 0.12	47 ± 8	155 ± 16 (n = 24)	CAM	50.7 ± 6.1

Note.
[a] Values used for dose rate and age calculations, with measured (field) water contents shown in parentheses.
[b] The final ages are those obtained from pIRIR290 signals. All the ages were calculated by subtracting the residual dose (7 ± 3 Gy) from corresponding D_e values. A relative error of 2% was included in the uncertainty on the final ages to allow for possible bias in the calibration of the laboratory beta source.

(31.3 ± 3 ka) is at the younger end of the range of published ages from the MP sites of Lusakert 1, Kalavan 2, and Bagratashen 1, which all have similar MP lithic technology, and are currently estimated to date to ~30–60 ka (Adler et al., 2012; Ghukasyan et al., 2011; Gasparyan et al., 2014; Egeland et al., 2016). Furthermore, all of the artifacts in Units 2b, 2a, and 1 were made with the same core

reduction techniques, and there is no change in techno-typology upwards through this part of the sequence (Glauberman et al. unpublished data). Consequently, there is no archaeological evidence to indicate human occupation at 7 ka, even in Units 2a, 1, and on the surface, and therefore, we suggest that the age estimated for Barozh-OSL-1 based on the dominant group (~31 ka) should

represent the depositional age of Unit 2b.

3.6. Biomarker analysis

Long-chain n-alkanes (nC$_{25}$-nC$_{35}$) with a high odd-over-even predominance (OEP, Equation (1)) are an important component of the epicuticular waxes of higher plants (Eglinton and Hamilton, 1967).

$$OEP = \frac{C_{25} + C_{27} + C_{29} + C_{31} + C_{33} + C_{35}}{C_{25} + C_{27} + C_{29} + C_{31} + C_{33} + C_{35}} \qquad (1)$$

This wax protects the plant from water loss, microbial attack and UV damage (Jetter et al., 2006). Studies have demonstrated that the relative abundance of n-alkanes produced by plants changes in response to environmental variables such as temperature and humidity (Bush and McInerney, 2013, 2015). It has also been demonstrated that the average chain length (ACL, Equation (2)) of n-alkanes extracted from modern sediments correlates to mean annual vapor pressure deficit (VPD, Equation (3)) (Eley and Hren, 2018).

$$ACL = \frac{25 \times C_{25} + 27 \times C_{27} + 29 \times C_{29} + 31 \times C_{31} + 33 \times C_{33} + 35 \times C_{35}}{C_{25} + C_{27} + C_{29} + C_{31} + C_{33} + C_{35}}$$
$$\qquad (2)$$

$$VPD = 1.3125 - \sqrt{14.1208 - 0.4629 \times ACL} \qquad (3)$$

Given that n-alkane molecules are resistant to degradation over long time scales (Schimmelmann et al., 1999) and their response to environmental variables, they are therefore a useful paleoclimate proxy. Previous work at Middle Paleolithic sites has employed these molecular proxies in direct association with archaeological materials to interpret paleoclimate (Krajcarz et al., 2010; Galván et al., 2014; Leierer et al., 2019; Connolly et al., 2019).

OEP values for all samples are above 3, indicating that lipids did not undergo significant microbial alteration (Table 5). The two samples from Unit 5 are similar to Unit 3 in their distribution of n-alkanes, with high ACL (range 29.71−30.02, mean 29.87) and a correspondingly high VPD (range 0.71−0.84, mean 0.77). The most abundant n-alkane homologue in these samples is n-C29, with the exception of the lowermost sample (75−80 cm), whose most abundant homologue is n-C31. The difference in both the ACL

Table 5
Long chain n-alkane concentration, odd-over-even predominance (OEP) and average chain length (ACL). Vapor pressure deficit (VPD) is reconstructed from ACL after Eley and Hren (2018).

Depth (cm below surface)	Unit	Concentration (ng/g)	OEP	ACL	VPD
0−5	1	363.11	6.90	30.13	0.89
5−10	2	220.31	4.08	29.14	0.52
10−15		327.99	4.17	29.04	0.49
15−20		282.47	3.89	28.75	0.41
20−25		151.08	3.60	28.50	0.35
25−30		167.69	3.52	28.23	0.29
30−35		116.88	3.59	28.13	0.26
35−40		65.81	3.47	28.14	0.27
40−45	3	18.81	3.24	29.31	0.57
45−50		15.71	3.83	29.59	0.66
50−55		25.23	6.76	30.50	1.27
55−60		28.73	6.81	30.20	0.93
60−65		22.67	4.97	29.61	0.67
65−70		16.67	4.33	29.73	0.71
70−75	5	28.49	5.18	29.71	0.71
75−80		37.68	5.32	30.02	0.84

(p < 0.001) and the VPD (p < 0.001) between Units 3 and 2 is statistically significant. An abrupt shift in n-alkane distribution occurs in Unit 2, with a lower ACL (range 28.13−29.14, mean 28.56), corresponding to a lower reconstructed VPD (range 0.26−0.52, mean 0.37). The most abundant n-alkane homologue in samples from Unit 2 is n-C25. n-alkane distributions in Unit 3 are similar to the modern A horizon (Unit 1), with a higher ACL (range 29.31−30.50, mean 29.82) and higher reconstructed VPD (0.57−1.27, mean 0.80) than Unit 2. Modern A horizon (Unit 1) n-alkanes have an ACL of 30.13. The most abundant n-alkane homologue is n-C31. Leaf lipid distributions are similar to other MP sites in the Armenian highlands (Brittingham et al., 2019), and reveal a changing environment during the presence of hominins at Barozh 12.

3.7. Artifact analysis

In total, 17,317 obsidian artifacts were recovered from 4.85 m^3 of excavated sediment from all trenches. All artifacts were ascribed to the MP on techno-typological grounds, for example, dominant unidirectional-convergent and unidirectional Levallois core reduction techniques. Levallois points, retouched Levallois points, Mousterian points, and single and double scrapers dominate the tool assemblages throughout the sequence (Fig. 10). The proximal ends of blanks and tools frequently bear evidence of secondary modification in the form of truncation and faceting. As such, the Barozh 12 MP artifacts appear similar to those from other MP sites dated to ~60−30 ka in Armenia (e.g. Lusakert 1, Bagratashen 1), Georgia (e.g. Ortvale Klde), and the northern Levant (e.g. Hummal, Umm El Tlel) (e.g. Adler, 2002; Golovanova and Doronichev, 2003; Adler and Tushabramishvili, 2004; Adler et al., 2006; Meignen and Tushabramishvili, 2006; Hauck, 2011; Moncel et al., 2013; Gasparyan et al., 2014; Boëda et al., 2015; Moncel et al., 2015; Glauberman et al., 2016). In all strata, all but the earliest stages of core reduction are represented to varying degrees. Tool (or retouch) frequency varies according to density among stratigraphic units (cf. Barton and Riel-Salvatore, 2014), indicating differential occupational intensity and changes in emphasis on tool production versus use and discard over time. No faunal material was encountered. The following analysis of artifact condition and vertical size distributions focus on Trenches 36A7, 47J1, and 47T1 (Tables 6 and 7).

3.7.1. Artifact breakage and damage

In Trenches 36A7, 47J1, and 47T1, high frequencies of fragmented artifacts occur in all strata (76.7−91.6%). The only notable change in breakage frequency within a stratigraphic unit is a decrease in broken flakes from lower to upper Unit 3 (Fig. 11). Lower Unit 3 has a higher frequency of broken artifacts than the uppermost gravelly Unit 1+2a.[1] The high frequency of broken artifacts recovered from lower Unit 3 could relate to higher energy deposition indicated by sands and fine pebbles at the bottom of the fining upward sequence. Otherwise, breakage patterns are relatively consistent throughout the stratigraphic sequence.

Artifact damage patterns closely mirror those of breakage (Fig. 10). The frequency of un-damaged artifacts is relatively constant from Unit 5 into lower Unit 3. However, the frequency of un-damaged artifacts increases from lower to upper Unit 3, then decreases again in Unit 2b. The uppermost Unit 1+2a has the highest frequency of severely damaged artifacts in the sequence, an observation which is consistent with the clast-supported deposit from which the artifacts were excavated. We conclude that artifact damage and breakage are not solely a result of hydraulic transport,

---

[1] In the lithics analyses, artifact data from reworked Units 1 and 2a have been combined into one analytical unit (Unit 1+2a).
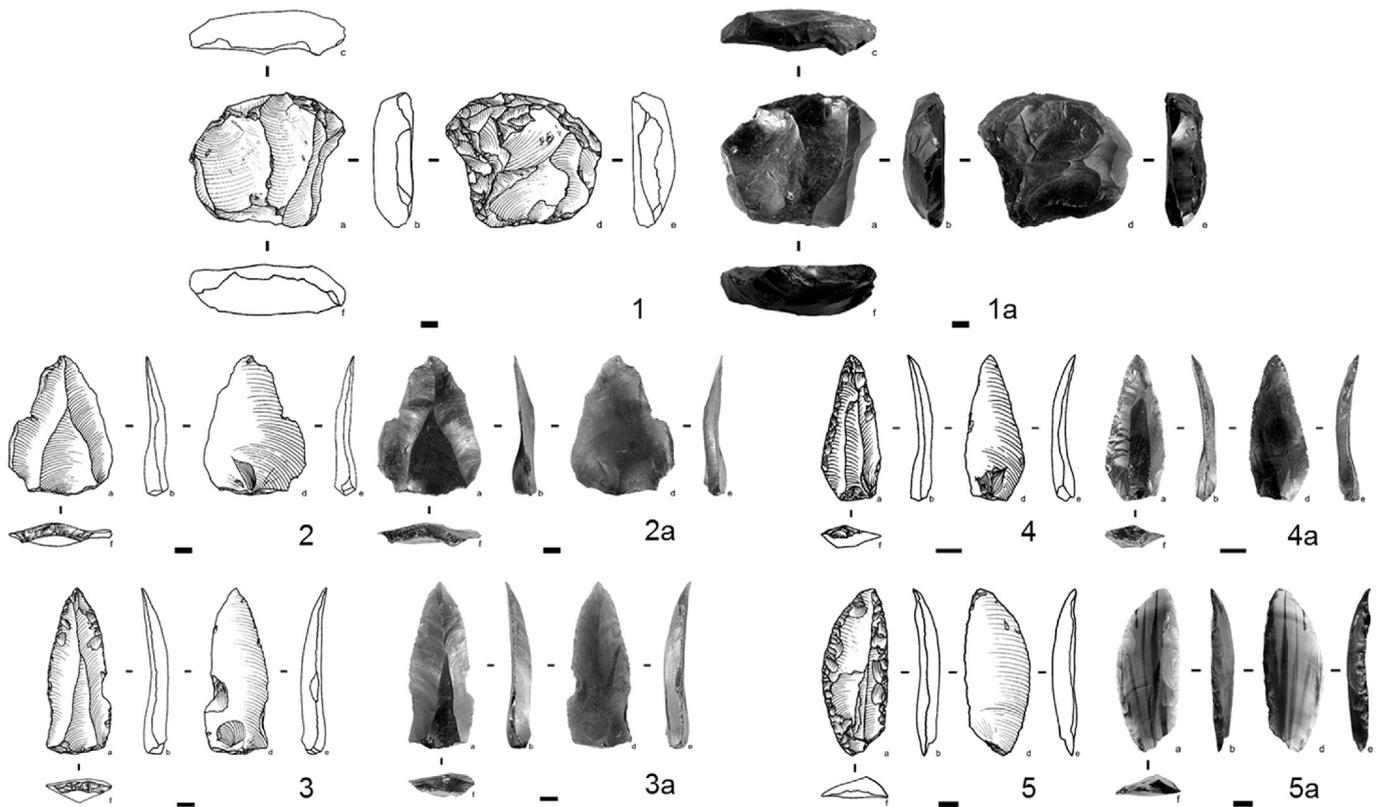
Fig. 10. Selected Middle Paleolithic obsidian artifacts from Barozh 12: 1-1a (after Glauberman et al., 2016). unidirectional-convergent Levallois core (Unit 1+2a); 2-2a. Levallois point (Unit 1+2a); 3-3a. retouched Levallois point (Unit 2b); 4-4a. retouched Levallois point (Unit 3); 5-5a. straight-convex double scraper (Unit 5). Scale bars = 1 cm.

and rather could result from the friability and brittleness of obsidian, and breakage *in-situ* due to trampling and sediment compaction (e.g. Gifford-Gonzalez et al., 1985; Pryor, 1988; Nielson, 1991; McBrearty et al., 1998; Eren et al., 2011; McPherron et al., 2014; Driscoll et al., 2016). Moreover, we cannot rule out artifact damage and breakage having occurred during manufacture and use.

3.7.2. Carbonate coatings

In arid to semi-arid conditions calcium carbonate coatings commonly form on clasts and artifacts as a result of $CaCO_3$ precipitation out of sediments and soils, and as a response to wetting and drying (Gile et al., 1966; Birkeland, 1999; Treadwell-Steitz and McFadden, 2000; Pustovoytov, 2002, 2003). In Units 3−5, carbonate crusts cover less than 40% of one surface of most artifacts, mainly their lower surfaces. This differs from the uppermost Units 1+2a and 2b, where the majority of artifacts are covered in carbonate crusts on both surfaces (Fig. 10). This pattern suggests that in Units 2b and 1+2a, carbonate precipitation is consistent with aridity and occurred at a more prolonged duration after artifact deposition (Gile et al., 1966; Treadwell-Steitz and McFadden, 2000; Pustovoytov, 2002, 2003). The difference in carbonate coverage between upper Unit 3 and Unit 2b indicates a sharp separation marked by the disconformity between these units. This likely divides recent pedogenic carbonate precipitation related to Holocene semi-arid climate and vegetation regime, from older and different prevailing aridity and vegetation regimes during the deposition of and pedogenesis within Units 5−3. This pattern is consistent with the results of sedimentology, micromorphology, and biomarker analysis presented earlier.

3.7.3. Artifact weathering

Artifacts made on siliceous rocks develop weathering rinds, or patina, in sub-aerial and buried contexts according to the prevailing geochemical conditions and humidity, pH, and temperature. The degree and symmetry of artifact weathering broadly represents the extent to which artifact surfaces were exposed to conditions that induce weathering (Röttlander, 1975; Burroni et al., 2002; Glauberman and Thorson, 2012; Thiry et al., 2014; Caux et al., 2018). Obsidian develops hydration rinds through the absorption of water due to similar factors that induce patina on siliceous rocks (Friedman et al., 1966; Anovitz et al., 2006; Anovitz et al., 2008). In the Barozh 12 sequence, patterns of artifact weathering vary between stratigraphic units (Fig. 10). For example, the artifacts from lower Unit 5 show significantly increased weathering severity and symmetry compared to upper Unit 5 ($\chi^2 = 8.96$, df = 3, p = 0.033), while no un-weathered artifacts were found in the unit. This pattern may relate generally to the increased humidity during the deposition of Unit 5 observed in biomarker analysis. Upper Unit 5 has a similar pattern of artifact weathering severity and symmetry to lower Unit 3 ($\chi^2 = 0.457$, df = 3, p = 0.928), commensurate with its similar grain size, the diffuse contact between upper Unit 5 and lower Unit 3 and probably similar post-depositional processes operating in these sub-units. Lower Unit 3 has more severely weathered artifacts compared to upper Unit 3, a property that may relate to downward mineral translocation associated with pedogenesis. However, upper and lower Unit 3 do not differ significantly in weathering category frequency ($\chi^2 = 6.12$, df = 3, p = 0.105). In upper Unit 3, the frequencies of severely weathered artifacts and those weathered on one side are significantly less than in overlying Unit 2b ($\chi^2 = 12.4$, df = 3, p < 0.006). This may result from a combination of lower soil humidity in upper Unit 3, in which

Table 6
Artifacts categorized according to class (core, blank, flake < 2 cm [maximum dimension], angular debris (Ang. debris), angular debris < 2 cm [maximum dimension]), and listed according to (sub) stratigraphic unit. Blank is utilized as a category because retouch was not always apparent on blanks due to carbonate coatings. Total * indicates the sample analyzed in Fig. 11.

36A7		Core			Blank			Flake < 2 cm			Ang. debris	Ang. debris < 2 cm	Total	Unit Total
Stratigraphic Unit	Depth	Complete	Broken	Total	Complete	Broken	Total	Complete	Broken	Total				
l+2a	0–20 cm	39	21	60	98	376	474	71	246	317	198	282	480	1331
2b	20–40 cm	18	13	31	69	297	366	21	159	180	155	154	309	886
3 Upper	40–60 cm		4	4	56	136	192	80	152	232	121	133	254	682
3 Lower	60–70 cm	1	2	3	26	96	122	10	174	184	48	165	213	522
5 Upper	70–80 cm	2	1	3	7	76	83	8	52	60	45	114	159	305
5 Lower	80–90 cm			0	6	11	17	3	19	22	9	27	36	75
Total		60	41	101	262	992	1254	193	802	995	576	875	1451	3801

47J1		Core			Blank			Flake < 2 cm			Ang. debris	Ang. debris < 2 cm	Total	Unit Total
Stratigraphic Unit	Depth	Complete	Broken	Total	Complete	Broken	Total	Complete	Broken	Total				
l+2a	0–30 cm	72	44	116	208	818	1026	36	334	370	632	312	944	2456
2b	30–40 cm	13	7	20	55	113	168	33	62	95	85	61	146	429
3 Upper	40–50 cm	1		1	24	130	154	5	103	108	28	12	40	303
3 Lower	50–60 cm	3		3	6	145	151	4	353	357	23	37	60	571
5 Upper	60–70 cm	2	1	3	46	73	119	23	140	163	57	74	131	416
5 Lower	70–80 cm			0	10	26	36	14	74	88	8	41	49	173
Total		91	52	143	349	1305	1654	115	1066	1181	833	537	1370	4348

47T1		Core			Blank			Flake < 2 cm			Ang. debris	Ang. debris < 2 cm	Total	Unit Total
Stratigraphic Unit	Depth	Complete	Broken	Total	Complete	Broken	Total	Complete	Broken	Total				
l+2a	0–40 cm	50	25	75	39	916	955		473	473	600	288	888	2391
2b	40–50 cm	4	5	9	35	155	190		176	176	28	14	42	417
3 Upper	50–60 cm	1	2	3	28	78	106	76	313	389	21	27	48	546
3 Lower	60–70 cm	2	1	3	11	84	95	46	331	377	18	41	59	534
5 Upper	70–80 cm	1		1	4	47	51	40	165	205	24	12	36	293
5 Lower	80–100 cm	1		1	7	25	32	17	53	70	10	13	23	126
Total		59	33	92	124	1305	1429	179	1511	1690	701	395	1096	4307

Total *		Core			Blank			Flake < 2 cm			Ang. debris	Ang. debris < 2 cm	Total	Unit Total
Stratigraphic Unit		Complete	Broken	Total	Complete	Broken	Total	Complete	Broken	Total				
l+2a		161	90	251	345	2110	2455	107	1053	1160	1430	882	2312	6178
2b		35	25	60	159	565	724	54	397	451	268	229	497	1732
3 Upper		2	6	8	108	344	452	161	568	729	170	172	342	1531
3 Lower		6	3	9	43	325	368	60	858	918	89	243	332	1627
5 Upper		5	2	7	57	196	253	71	357	428	126	200	326	1014
5 Lower		1	0	1	23	62	85	34	146	180	27	81	108	374
Total		210	126	336	735	3602	4337	487	3379	3866	2110	1807	3917	12456

49H1		Core			Blank			Flake < 2 cm			Ang. debris	Ang. debris < 2 cm	Total	Unit Total
Stratigraphic Unit	Depth	Complete	Broken	Total	Complete	Broken	Total	Complete	Broken	Total				
1 + 2	0–25 cm				1	5	6	1	5	6	16	16	32	44
3	25–50 cm	3		3	9	23	32	5	18	23	15	6	21	79
4a Upper	50–60 cm													
4a Lower	60–70 cm				1	4	5		1	1				6
4b	70–8 5 cm				5	7	12		1	1				13
5	85–100 cm				1	2	3		1	1			1	5
Total		3		3	17	41	58	6	26	32	32	22	54	147

Table 7
Excavated volume, numbers of artifacts, and artifact density (artifacts/m³) according to trench and stratigraphic unit. 49H1 not included in analyses shown in Fig. 11.

	36A7			47J1			47T1			Total			49H1		
	Volume (m³)	n artifacts	Density	Volume (m³)	n artifacts	Density	Volume (m³)	n artifacts	Density	Volume (m³)	n artifacts	Density	Volume (m³)	n artifacts	Density
Unit 1+2a	0.2	1331	6655	0.3	2456	8187	0.4	2391	5978	0.9	6178	6864	0.25	44	176
Unit 2b	0.2	886	4430	0.1	429	4290	0.1	417	4170	0.4	1732	4330	0.25	79	316
Unit 3 Upper	0.2	682	3410	0.1	303	3030	0.1	546	5460	0.4	1531	3828	0.1	0	0
Unit 3 Lower	0.1	522	5220	0.1	571	5710	0.1	534	5340	0.3	1627	5423	0.1	6	60
Unit 5 Upper	0.1	305	3050	0.1	416	4160	0.1	293	2930	0.3	1014	3380	0.15	13	87
Unit 5 Lower	0.1	75	750	0.1	173	1730	0.2	126	630	0.4	374	935	0.15	5	33
Total	0.9	3801	4223	0.8	4348	5435	1	4307	4307	2.7	12456	4613	1	147	147

Artifact size	Unit 1+2a (n = 6178)	Unit 2b (n = 1732)	Unit 3a Upper (n = 1531)	Unit 3a Lower (n = 1627)	Unit 5 Upper (n = 1014)	Unit 5 Lower (n = 374)
Upper CI	3.6	3.54	2.73	2.36	2.58	2.43
Mean	3.55	3.46	2.66	2.31	2.5	2.31
Lower CI	3.5	3.37	2.59	2.26	2.42	2.18
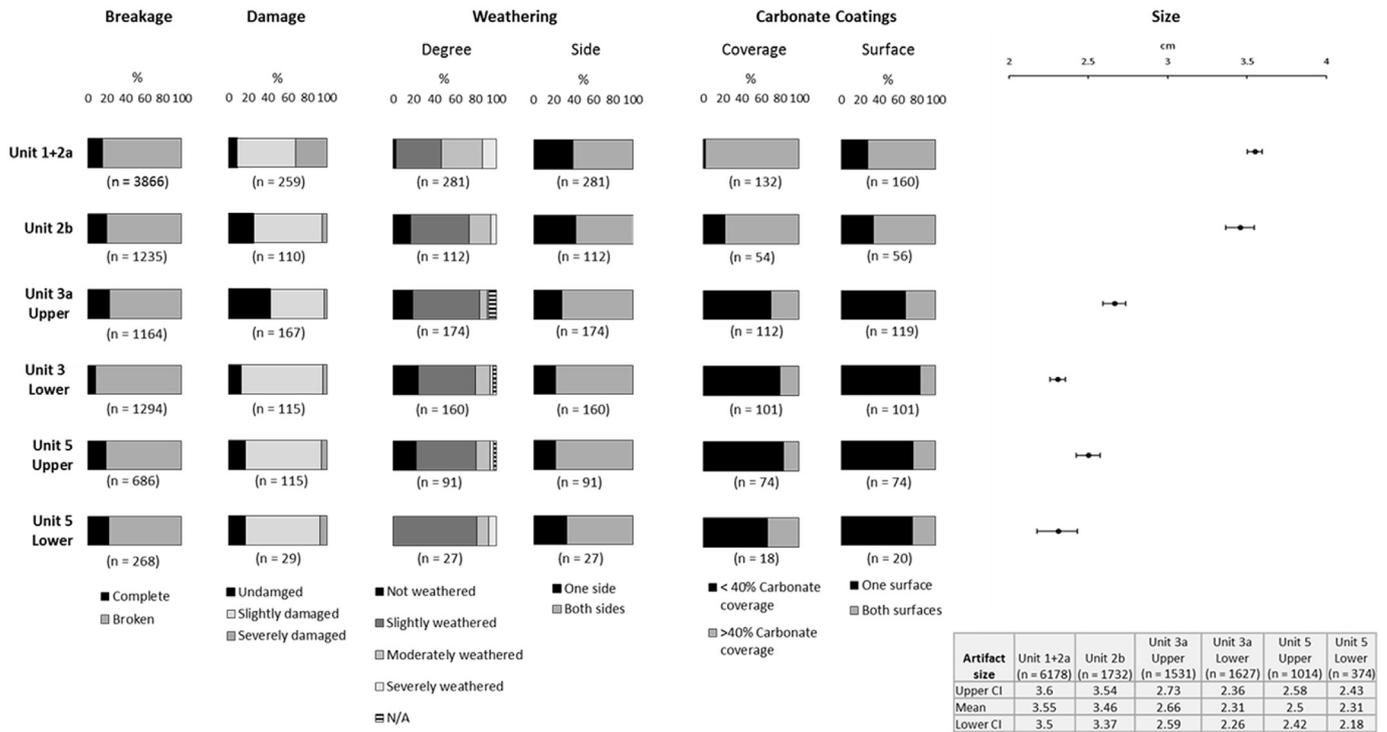
Fig. 11. Frequencies of artifact preservation variables, and mean artifact size (maximum dimension) with bootstrapped upper and lower 95% confidence intervals (CI) according to stratigraphic (sub-)units. Non-overlapping interval ranges indicate significant differences. Breakage data from cores, blanks, flakes < 2 cm in maximal dimensions, angular debris excluded. Artifact size data from all complete and broken artifacts (see Table 6 for further details).

weathering may have been less intense than in Unit 2b but progressed on all artifact surfaces due to a homogenous matrix that is conducive to mineral translocation and also a consistent pH. The lithic artifact assemblages from the uppermost Units 2b and 1+2a have higher frequencies of moderately and severely weathered artifacts than other units. However, Unit 2b has a mix of weathering categories and a higher frequency of un-weathered artifacts than Unit 1+2a. In both strata, ~40% of artifacts are weathered on one side only. Asymmetrical weathering may have occurred *in-situ* on artifacts lying flat prior to colluvial reworking in Unit 1+2a. In Unit 2b, asymmetrical weathering in a relatively fine-grained alluvial context suggests that artifacts remained in a flat position during weathering associated with soil humidity and variation in micro-local geochemical conditions.

3.7.4. Artifact size distributions

Artifact size sorting due to hydraulic movement has been demonstrated experimentally and has also been tested on archaeological assemblages (e.g. Schick, 1986, 1987; Petraglia and Potts, 1994; Bertran et al., 2012, Sitzia et al., 2012). In this study, we utilized Schick's (1984, 1987) experimental data, as they were collected on artifacts that were treated using comparable methods to those employed at Barozh 12, including the screening of archaeological sediments through 5 mm mesh and linear artifact measurements using calipers. Schick (1987) and Bertran et al. (2012) include complete and broken artifacts in their analyses of size sorting. The data we analyze here therefore includes all artifact classes (Table 6) and both complete and broken artifacts. It is worth noting that lithic raw material type and different experimental artifact manufacture techniques (e.g. replicating Oldowan and Acheulean artifacts [Schick, 1987] and discoidal and Levallois blank production [Bertran et al., 2012]) can produce minor variation in resulting artifact and debris size distributions. However, Bertran

et al. (2012) show that, overall, differences in core reduction techniques and raw materials do not tend to greatly affect artifact size sorting comparisons with archaeological assemblages (Bertran et al., 2012). In undisturbed, experimentally replicated core reduction and tool manufacture datasets, artifacts <2 cm and small flaking debris (SFD), comprise ~60−80% of assemblages. SFD has been shown to be more susceptible to hydraulic displacement than larger and thicker artifacts (Schick, 1986, 1987, Kuman and Field, 2009; Lotter et al., 2016).

At Barozh 12, artifact size generally increases upwards through the sequence (Fig. 11), while vertical artifact size distributions show distinct differences between and within stratigraphic (sub)units. Artifacts increase in mean size upwards within Units 3 and 5, but only do so significantly in Unit 3. The stratigraphic disconformity between Unit 3 and Unit 2b marks a substantial increase in mean artifact dimensions. Artifacts in Units 2b and 1+2a are significantly larger on average than artifacts from underlying strata (Fig. 11).

Comparison of distribution curves of artifact maximal dimensions for assemblages recovered from squares 47J1, 47T1, and 36A7 at Barozh 12 and Schick's (1987) mean distribution of 107 undisturbed experimental assemblages shows differences among strata (Fig. 12A). Artifact size distribution patterns in stratigraphic Units 5−3 are consistent with those observed at other sites in low-energy alluvial contexts that indicate minimal disturbance and size sorting of artifacts, and that knapping occurred in the vicinity of the excavated area (e.g. Schick, 1984; Bertran et al., 2012; Hovers et al., 2014; Pei et al., 2014; Li et al., 2016; Lotter et al., 2016; Li et al., 2018). Units 1+2a and 2b have an upwards trend of increasing artifact size thereby suggesting winnowing of artifacts <2 cm in maximal dimensions.

We also compared artifact size class frequencies from Barozh 12 with replicated assemblages placed in different fluviatile depositional settings, that were subsequently excavated and analyzed
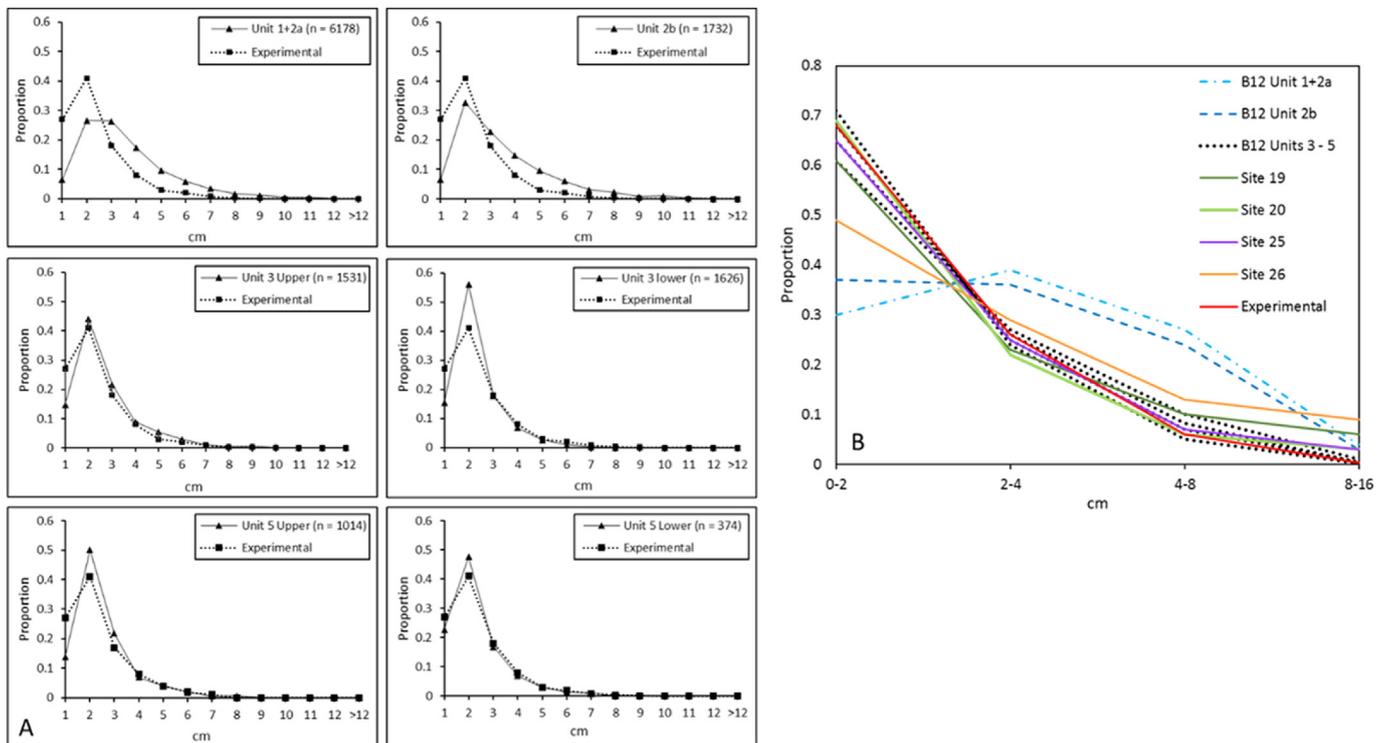
Fig. 12. (A) Comparing artifact size classes from Barozh 12 by stratigraphic unit from Trenches 36A7, 47T1, and 47J1 (data from all complete and broken artifacts, Table 6) with mean distributions from 107 undisturbed experimental assemblages (Schick, 1987). (B) Comparing artifact size class frequencies from Barozh 12 (B12) Units 1+2a, 2b (light blue and blue) and Units 3–5 (black dotted lines) with experimental results in varying contexts: undisturbed (Schick, 1987; red); Site 19: channel sand bar (Schick, 1984: 324; dark green); Site 20: channel bank (Schick, 1984: 331); Site 25: levee (Schick, 1984: 365; purple); Site 26: sand bar in moderate sized channel (Schick, 1984: 368; orange) (after Hovers et al., 2014). (For interpretation of the references to color in this figure legend, the reader is referred to the Web version of this article.)

after disturbance (Schick, 1984). Fig. 11B shows that artifact size frequency distributions from Units 5–3 all resemble those from Schick's (1984) data on assemblages reworked in levee and sandy stream channel bank and bar contexts. However, the artifact size frequency distributions in Units 5–3 best approximate the mean size distribution for undisturbed experimental assemblages (Schick, 1986, 1987), and appear less winnowed than the sandy channel and bar contexts. It is noteworthy that the Levallois dominant artifact assemblages made of fine-grained and brittle obsidian analyzed here closely resemble Schick's (1986, 1987) experimental data compiled for Oldowan and Acheulian artifact replications on coarse-grained, less brittle basalt. Units 2b and 1+2a fall well outside the size distribution of experimental artifact assemblages recovered from channel and stream side deposits, potentially indicating reworking by non-fluvial processes such as colluviation or other slope processes.

Lower Unit 5 appears less winnowed than upper Unit 5 based on reduced frequency of artifacts <2 cm, which may indicate reworking in the upper part of the unit associated with onset of relatively high energy deposition of sandy, pebbly sediments associated with the formation of lower Unit 3. This is commensurate with the diffuse contact and similar grain size of the upper part of Unit 5 and lower part of Unit 3. The artifact assemblage from lower Unit 3 appears more winnowed (Fig. 12A) and artifacts are more damaged and broken than the assemblage from upper part of that unit (Fig. 11). This coincides with the fining upward sequence indicating a decrease in depositional energy during the formation of Unit 3.

In summary, these analyses suggest that the artifact assemblages from Units 5–3 are comparatively less disturbed than the uppermost units, and were subject to the mild winnowing of artifacts <2 cm that is expected in fluvial contexts (e.g. Bertran et al., 2012; Sitzia et al., 2012; Hovers et al., 2014). Increase in size upwards within stratigraphic (sub)Units 5 and 3 (Fig. 11) suggests downward vertical migration of artifacts, possibly due to bioturbation, pedogenesis, and trampling (Vermeersch and Bubel, 1997; McBrearty et al., 1998), albeit that no large krotovinas or burrows were observed in the field. The disconformity observed at the contact of Units 2b and 3 likely represents a hiatus in artifact and sediment deposition, or the removal of both sediment and artifacts. The artifact assemblages recovered from Units 2b and 1+2a underwent moderate to severe disturbance, likely involving transport and re-deposition by alluvial and colluvial processes.

At present, we conclude that artifact assemblages in Units 5–3 have been minimally disturbed by hydraulic movement and therefore represent the best material with which to reconstruct hominin behavior. Comparison of artifact size distributions with Schick's (1984) experimental data suggests that artifacts in these units were deposited in levee, overbank, or proximal floodplain settings, an interpretation that is consistent with the granulometry and micromorphology results. Units 1+2a represent winnowed and disturbed assemblages in reworked deposits that were later deflated, consolidating larger artifacts and clasts.

4. Discussion

4.1. Formation of the Barozh 12 sequence

Using the IRSL chronology, sedimentological, archaeological, and biomarker evidence described earlier, it is possible to build a model of site formation processes at Barozh 12. Subsequent to the emplacement of the basal ignimbrite deposits ~650 ka (Gevorgyan

et al., 2018), there is evidence for at least one phase of relative landscape stability, which resulted in the pedogenic modification of the upper part of the ignimbrite. The earliest preserved occupations at the site are indicated by artifacts recovered from this weathered ignimbrite deposit (Unit 5). Aside from evidence of breakage and slight edge damage, there was minimal artifact disturbance by reworking and winnowing (artifacts < 2 cm) in this context (Unit 5), and analysis of biomarkers indicates a humid − semi-arid environment.

The onset of sediment deposition at the site, as represented by the earliest alluvial strata, occurred ~60−50 ka. Stream activity at the locality resulted in the deposition of both overbank and channel deposits at the site. These sediments contain a mixture of volcanogenic material, likely derived from the basal ignimbrite and material elsewhere in the catchment indicating transport of material from outside of the Barozh 12 locale. The absence of imbricated clasts within Units 4a and 4b preclude an assessment of flow direction, however, we hypothesize that this material was deposited from southward trending streams flowing from the Aragats neovolcanic area into the Ararat Depression. Associated with this phase of alluvial activity were several phases of incipient pedogenesis, likely in a semi-arid environment and accompanied by a fluctuating water table. Analysis of artifact size distribution indicates that artifacts recovered from Unit 3 were only minimally affected by fluvial winnowing and post-depositional reworking in an overbank or floodplain context. These intact archaeological deposits indicate hominins occupied this locality throughout the alluvial deposition and pedogenic alteration of the Unit 3 sediments.

Sedimentological, micromorphological, and chronological data from Trench 36A7 indicate a hiatus between the deposition of Units 3 and 2, which, based on the differences in IRSL age estimates between Units 3 and 2b, may represent an interval of approximately 20 kyr. We hypothesize that during this interval, there was a shift to greater aridity, resulting in the transportation, deposition and subsequent deflation of fine-grained material by aeolian processes. This interpretation is supported by the presence of gypsic features in Unit 3, which would require an extra-local source of sulfur to enable precipitation. Furthermore, artifactual evidence from the upper part of Unit 3 and Unit 2b indicates a relatively high frequency of damage and weathering, consistent with sub-aerial reworking of material. Based on our current evidence, the source of the aeolian material cannot be elucidated. However, there is evidence for lower water levels and the sub-aerial exposure of sulphide-rich lake sediments in the Black Sea during MIS 3 (Lericolais et al., 2007; Wegworth et al., 2016), and which may have provided a source. A further source may have been the Ararat Depression. However, based on the currently limited evidence from the area, the timing and duration of lake development in the Ararat Depression remain ambiguous.

A second phase of alluvial deposition (Unit 2b) at approximately 31 ka followed the deposition and subsequent deflation of aeolian material, the former was characterized by overbank sedimentation and incipient pedogenesis with colluvial processes also contributing to sediment input, albeit at the end of the alluvial cycle. Results of the *n*-alkane analysis provide evidence for a more humid environment associated with the deposition of Unit 2 than in Units 3 and 5, data that are also in line with the micromorphological evidence. The notable increase in mean artifact size from Unit 3 to Unit 2b (Fig. 11) is likely related to reworking by fluvial processes and moderate sorting and winnowing of the smallest artifacts (<2 cm) in Unit 2b (Figs. 11 and 12). Weak pedogenesis is also observed in this unit, while biomarkers indicate that the artifacts in Unit 2b were deposited during a return to a more humid − semi-arid environment.

Incision by southward trending streams occurred following the

deposition of the alluvial sediments and resulted in the sustained subaerial exposure of the Barozh 12 deposits and, in all likelihood, the formation of the dissected plateau that is present today. This fluvial incision was most likely tectonically controlled, and a result of a combination of regional uplift, which is estimated to range from 0.2 to 0.3 mm yr^{-1} (Mitchell and Westaway, 1999), and subsidence of the Ararat Depression. Associated with the incision episode was pedogenesis and the formation of the modern soil profile (Unit 1). Clast-rich Units 1+2a shows evidence of higher energy reworking and colluvial (re)deposition under humid − semi-arid conditions (Unit 2a), followed by deflation and Holocene soil formation (Unit 1). Artifacts were more severely reworked in this unit (Unit 1+2a), indicated by increased damage, weathering severity, and the relative absence of artifacts <2 cm in maximal dimensions (Figs. 11 and 12).

4.2. Regional climatic and environmental context

Sedimentology and the biomarker evidence in the Barozh 12 sequence provide a record of broad fluctuations in humidity during MIS 3 that is consistent with other regional paleoclimate data. For example, biomarker and authigenic carbonate isotope records from Lake Van show high $\delta^{18}O$ and δD values during the last glacial period (MIS 4−2, c. 71−11.7 ka), suggesting arid conditions (Stockhecke et al., 2016; Randlett et al., 2017). Moreover, pollen records from Lake Van (Litt et al., 2014) and Lake Urmia (Djamali et al., 2008) for the same period are dominated by non-arboreal pollen, suggesting an open landscape. However, regional data also demonstrate that the aridity of the last glacial period in these localities was punctuated by intervals of more humid conditions. For example, lake levels in Lake Van, Lake Urmia and Lake Zeribar are generally high at 30−35 kya, suggesting a humid environment (Snyder et al., 2001; Djamali et al., 2008; Çağatay et al., 2014). Speleothem records from Anatolia at Sofular and Dim Caves, also provide evidence for increased regional moisture during MIS 3 (Fleitmann et al., 2009; Badertscher et al., 2011; Ünal-İmer et al., 2015). These broad shifts between intervals of arid and relatively humid conditions are reflected in the Barozh 12 sequence. High reconstructed VPD values in Unit 3 and Unit 5 reflect an interval of enhanced aridity between 45 and 65 ka, and perhaps contemporaneous with a shift to increased evaporation in the Lake Van $\delta^{18}O$ record (Fig. 13). Conversely, lower reconstructed VPD in Unit 2b of the Barozh sequence is indicative of more humid conditions around 33−28 ka, a period that is coincident with an interval of increased precipitation in the Lake Van $\delta^{18}O$ record.

However, superimposed on these broad shifts are millennial-scale fluctuations, which would have had significant effects of landscape stability. Indeed, the latter are shown clearly in the Lake Van Ca/K record which acts a proxy for detrital inputs into the lake, and thus soil development and erosion in the catchment (Fig. 13B). Rapid fluctuations in the Ca/K record between 50 and 30 ka suggest fluctuating detrital inputs and thus landscape instability during this period. It is important to note, that this interval coincides with the sedimentary hiatus recorded in the Barozh 12 sequence and it may therefore be the case that these changing conditions are linked to intervals of aeolian deposition and deflation at the latter locale. The contemporaneous shifts in environments observed at Barozh 12 and records such as Lake Van, suggests that correlations are possible between local, fragmentary terrestrial archives and regional, continuous paleoenvironmental sequences.

4.3. IRSL age estimates and regional MP chronology

At Barozh 12 we document unchanging lithic technology
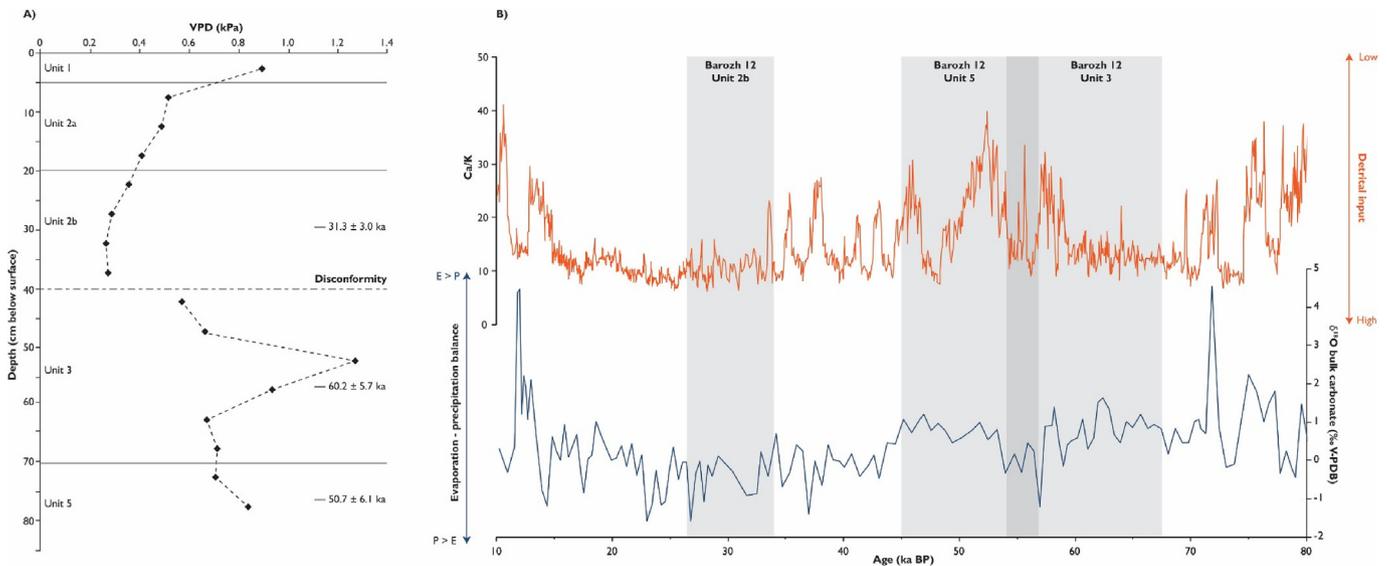
Fig. 13. (A) reconstructed VPD values from the Barozh 12 sequence. (B) Ca/K ratios (orange) and $\delta^{18}O$ bulk carbonate values (blue) for the interval 80-10 ka from Lake Van (Pickarski et al., 2015). Also shown are the measured ages of Barozh 12 Units 2b, 3 and 5. Grey boxes represent age range of Units based on 2 σ uncertainty. Note the slight age reversal between Unit 5 and Unit 3, however the ages overlap at 2 σ uncertainty. (For interpretation of the references to color in this figure legend, the reader is referred to the Web version of this article.)

through a sequence dating between ~60 and 50 ka and 31 ka. This latter date can be viewed as a *terminus post quem* for the archaeological material recovered from the moderately reworked, uppermost Unit 1+2a. However, it may also represent a Pleistocene re-deposition age. Potential problems have been reported with IRSL and OSL age under-estimation in Armenia, likely associated with the volcanic environment (e.g. Wolf et al., 2016; Egeland et al., 2016). In this study we utilized pIRIR methods to avoid potential age estimation problems. Given this, and despite reworking of sediments above the uppermost IRSL sample location (Barozh-OSL-1), we presently consider this date to be accurate pending further testing with other chronometric methods. The occupational time span at Barozh 12 coincides with that based on preliminary ages for MP deposits at the Lusakert Cave-1 site in the Hrazdan River Valley, ~80 km to the east; the Bagratashen-1 open-air site in the Debed River valley to the north; and the Kalavan-2 open-air site on the northern flanks of the Areguni Mountains north of Lake Sevan to the northwest (Adler et al., 2012; Ghukasyan et al., 2011; Gasparyan et al., 2014; Egeland et al., 2016).

5. Conclusion

Few MP open-air sites in Armenia have undergone extensive geoarchaeological, chronometric or paleoenvironmental examination. This study represents the first published account of any open-air Paleolithic site in the Armenian highlands where detailed taphonomic, geoarchaeological, and biomarker studies have been combined within an absolute chronometric framework to understand site formation processes, human activity, and their relationship with climate change. The results of site formation analysis greatly improve our view of diachronic hominin occupations and behaviors at Barozh 12. Artifacts were deposited on relatively stable surfaces, or in low-energy depositional settings. Assessment of variation in artifact assemblage composition across strata therefore provides detailed data on variability in hominin mobility, land use, and technological organization at this site, and in relation to other chronologically contemporaneous MP sites in the region. These behaviors can now be contextualized within the regional climatic and environmental setting.

In the absence of preserved faunal and plant macrofossil remains, artifact preservation and size distribution data, sedimentological, chronometric, and biomarker evidence show that Barozh 12 was occupied repeatedly at the beginning and end of MIS 3 (60.2 ± 5.7–50.7 ± 6.1 ka and 31.3 ± 3.0 ka) and under changing depositional and climatic conditions. Fluctuations in humidity and landscape stability inferred at Barozh 12 are consistent with data from regional paleoenvironmental records including from sediment cores taken from Lake Van, ~200 km away.

Hominins equipped with MP technology frequently re-visited this streamside locality during MIS 3 due to its close proximity to water, abundant obsidian toolstone, and position at the topographic junction of the Ararat basin − Araxes River valley, and the Mt Arteni and Mt Aragats uplands. The artifact assemblages deposited throughout the Units 5−3 alluvial sequence are relatively well-preserved, while those in the uppermost stratigraphic units have underdone moderate post-depositional disturbance. Amidst regional, millennial-scale climate variability, and changing aridity regimes of MIS 3, the Barozh 12 locality was likely a 'persistent place' (cf. Schlanger, 1992) in MP hominin settlement systems. Despite very different climate and aridity regimes in the early (Units 5−3) and late (Unit 2b and 1+2a) stages of MIS 3, hominins frequently re-occupied this site. This indicates that the resources available in the surroundings of Barozh 12 were sufficient to counteract any risks associated with variable climate regimes. Furthermore, the high density of artifacts throughout the sequence indicates that regional MP settlement systems were well established in this part of the Armenian highlands and the Southern Caucasus during those parts of MIS 3 when Barozh 12 was occupied. Obsidian sourcing using pXRF analysis 'tracks' hunter-gatherer mobility, and published data show that hominins at Barozh 12 made obsidian artifacts and transported them to numerous other sites, including Lusakert 1 cave in the Hrazdan River valley (Frahm et al., 2014; Frahm et al., 2016; Glauberman et al., 2016). This pattern similarly appears in the Lower Paleolithic at Nor Geghi 1, also in the Hrazdan valley (Adler et al., 2014), further demonstrating the long-term importance of Barozh 12 and the Arteni volcanic complex to different hominins who practiced extensive regional mobility systems throughout the Paleolithic. Considering

the growing number of chronometrically dated MP sites in Armenia, Barozh 12 represents a key open-air locality with a record of regional MP settlement dynamics during a crucial period for the study of human evolution and population dynamics in southwest Asia.

CRediT authorship contribution statement

Acknowledgements

Appendix A. Supplementary data

References

Adler, D.S., 2002. Late Middle Palaeolithic Patterns of Lithic Reduction, Mobility, and Land Use in the Southern Caucasus. Unpublished PhD thesis, Department of Anthropology, Harvard University, Cambridge.

Adler, D.S., Bar-Oz, G., Belfer-Cohen, A., Bar-Yosef, O., 2006. Ahead of the game: Middle and upper paleolithic hunting behaviors in the southern Caucasus. Curr. Anthropol. 47, 89−118.

Adler, D.S., Tushabramishvili, N., 2004. Middle paleolithic patterns of settlement and subsistence in the southern Caucasus. In: Conard, N.J. (Ed.), Settlement Dynamics of the Middle Paleolithic and Middle Stone Age, vol. II. Kerns Verlag, Tübingen, pp. 91−133.

Adler, D.S., Yeritsyan, B., Wilkinson, K., Pinhasi, R., Bar-Oz, G., Nahapetyan, S., Bailey, R., Schmidt, B.A., Glauberman, P., Wales, N., Gasparyan, B., 2012. The hrazdan gorge palaeolithic project, 2008−2009. In: Avetisyan, P., Bobokhyan, A. (Eds.), Archaeology of Armenia in Regional Context. Institute of Archaeology and Ethnography, Armenian Academy of Sciences, Yerevan, pp. 21−37.

Adler, D.S., Wilkinson, K.N., Blockey, S., Mark, D.F., Pinhasi, R., Schmidt-Magee, B.A., Nahapetyan, S., Mallol, C., Berna, F., Glauberman, P.J., Raczynski-Henk, Y., Wales, N., Frahm, E., Jöris, O., MacLeod, A., Smith, V.C., Cullen, V.L., Gasparyan, B., 2014. Early Levallois technology and the lower to Middle palaeolithic transition in the southern Caucasus. Science 345, 1609−1613.

Akazawa, T., Aoki, K., Bar-Yosef, O. (Eds.), 1998. Neandertals and Modern Humans in Western Asia. Plenum Press, New York.

Anovitz, L.M., Riciputi, L.R., Cole, D.R., Fayek, M., Elam, J.M., 2006. Obsidian hydration: a new paleothermometer. Geology 34, 517−520.

Anovitz, L.M., Cole, D.R., Fayek, M., 2008. Mechanisms of rhyolitic glass hydration below the glass transition. Am. Mineral. 93, 1166−1178.

Aspinall, W.P., Charbonnier, S., Connor, C.B., Connor, L.J.C., Costa, A., Courtland, L.M., Delgado Granados, H., Godoy, A., Hibino, K., Hill, B.E., Komorowski, J.C., McNutt, S., Meliksetian, K., Morita, S., Newhall, C., Samaddar, S.K., Savov, I.P., Self, S., Uchiyama, Y., Wilson, T., Yamamoto, T., Watanabe, K., 2016. Volcanic Hazard Assessments for Nuclear Installations: Methods and Examples in Site Evaluation. International Atomic Energy Agency, Vienna (IAEA-TECDOC-1795).

Avagyan, A., Sosson, M., Sahakyan, L., Sheremet, Y., Vardanyan, S., Martirosyan, M., Muller, C., 2018. Tectonic evolution of the northern margin of the cenozoic Ararat basin, lesser Caucasus, Armenia. J. Petrol. Geol. 41, 495−511.

Badertscher, S., Fleitmann, D., Cheng, H., Edwards, R.L., Gokturk, O.M., Zumbuhl, A., Leuenberger, M., Tuysuz, O., 2011. Pleistocene water intrusions from the mediterranean and caspian seas into the Black Sea. Nat. Geosci. 4, 236−239.

Barton, M., Riel-Salvatore, J., 2014. the formation of lithic assemblages. J. Archaeol. Sci. 46, 334−352.

Bar-Yosef, O., Belfer-Cohen, A., 2013. Following Pleistocene road signs of human dispersals across Eurasia. Quat. Int. 285, 30−43.

Birkeland, P.W., 1999. Soils and Geomorphology. Oxford University Press, New York.

Bertran, P., Lenoble, A., Todisco, D., Desrosiers, P.M., Sørensen, M., 2012. Particle size distribution of lithic assemblages and taphonomy of Palaeolithic sites. J. Archaeol. Sci. 39, 3148−3166.

Blott, S.J., Pye, K., 2001. GRADISTAT: a grain size distribution and statistics package for the analysis of unconsolidated sediments. Earth Surf. Process. Landforms 26 (11), 1237−1248.

Boëda, É., Bonilauri, S., Kaltnecker, E., Valladas, H., Al-Sakhel, H., 2015. Un débitage lamellaire au Proche-Orient vers 40,000 ans cal BP. Le site d'Umm el Tlel, Syrie centrale. L'anthropologie 119, 141−169.

Bordes, J.G., 2003. Lithic taphonomy of the châtelperronian/aurignacian interstratifications in Roc de Combe and Le piage (Lot, France). In: Zilhão, J., d'Errico, F. (Eds.), The Chronology of the Aurignacian and of the Transitional Technocomplexes. Dating, Stratigraphies, Cultural Implications. Proceedings of Symposium 6.1 of the XIVth Congress of the UISPP (University of Liège, Belgium, September 2-8, 2001), vol. 33. Trabalhos de Arqueologia, pp. 223−244.

Bretzke, K., Conard, N.J., 2017. Not just a crossroad: population dynamcis and changing material culture southwestern Asia during the late Pleistocene. Curr. Anthropol. 58. S000 1-14.

Brittingham, A., Hren, M., Hartman, G., 2017. Microbial alteration of the hydrogen and carbon isotopic composition of n-alkanes in sediments. Org. Geochem. 107, 1−8.

Brittingham, A., Hren, M.T., Hartman, G., Wilkinson, K.N., Mallol, C., Gasparyan, B., Adler, D.S., 2019. Geochemical evidence for the control of fire by Middle palaeolithic hominins. Sci. Rep. 1−7.

Bullock, P., Fedoroff, N., Jongerius, A., Stoops, G., Tursina, T., 1985. Handbook for Soil Thin Section Description. Waine Research, Wolverhampton, UK.

Burroni, D., Donahue, D.E., Pollard, M.A., Mussi, M., 2002. The surface alteration features of flint artifacts as a record of environmental processes. J. Archaeol. Sci. 29, 1277−1287.

Bush, R.T., McInerney, F.A., 2013. Leaf wax n-alkane distributions in and across modern plants: implications for paleoecology and chemotaxonomy. Geochem. Cosmochim. Acta 117, 161−179.

Bush, R.T., McInerney, F.A., 2015. Influence of temperature and C4 abundance on n-

alkane chain length distributions across the central USA. Org. Geochem. 79, 65–73.

Çağatay, M.N., Öğretmen, N., Damcı, E., Stockhecke, M., Sancar, Ü., Eriş, K.K., Özeren, S., 2014. Lake level and climate records of the last 90 ka from the Northern Basin of Lake Van, eastern Turkey. Quat. Sci. Rev. 104, 97–116.

Caux, S., Galland, A., Queffelec, A., Bordes, J.G., 2018. Aspects and characterization of chert alteration in an archaeological context: a qualitative to quantitative pilot study. J. Archaeol. Sci.: Reports 20, 210–219.

Chernyshev, I.V., Lebedev, V.A., Arakelyants, M.M., Jrbashyan, M.T., Gukasyan, Y.G., 2002. Quaternary geochronology of the Aragats volcanic center, Armenia: evidence from K–Ar dating. Dokl. Earth Sci. 384, 393–398.

Connolly, R., Jambrina-Enríquez, M., Herrera-Herrera, A.V., Vidal-Matutano, P., Fagoaga, A., Marquina-Blasco, R., Marin-Monfort, M.D., Ruiz-Sánchez, F.J., Laplana, C., Bailon, S., Pérez, L., Leierer, L., Hernández, C.M., Galván, B., Mallol, C., 2019. A multiproxy record of palaeoenvironmental conditions at the Middle Palaeolithic site of Abric del Pastor (Eastern Iberia). Quat. Sci. Rev. 225, 106023.

Dearing, J.A., 1999. Magnetic susceptibility. In: Walden, J., Oldfield, F., Smith, J. (Eds.), Environmental Magnetism; a Practical Guide. Technical Guide No. 6. Quaternary Research Association, London, pp. 35–62.

Dennell, R., 2008. The Palaeolithic Settlement of Asia. Cambridge University Press, Cambridge.

Dennell, R., Petraglia, M.D., 2012. The dispersal of Homo sapiens across southern Asia: how early, how often, how complex? Quat. Sci. Rev. 47, 15–22.

Dennell, R., 2017. Human colonization of Asia in the Late Pleistocene: the history of an invasive species. Curr. Anthropol. 58 (S17), S383–S396.

Djamali, M., de Beaulieu, J.L., Shah-hosseini, M., Andrieu-Ponel, V., Ponel, P., Amini, A., Akhani, H., Leroy, S.A.G., Stevens, L., Lahijani, H., Brewer, S., 2008. A late Pleistocene long pollen record from Lake Urmia, NW Iran. Quat. Res. 69, 413–420.

Driscoll, K., Alcaina, J., Éguez, N., Mangado, X., Fullola, J.M., Tejero, J.M., 2016. Trampled under foot: a quartz and chert human trampling experiment at the Cova del Parco rock shelter, Spain. Quat. Int. 424, 130–142.

Durand, N., Curtis Monger, H., Canti, M.G., 2010. Calcium carbonate features. In: Stoops, G., Marcelino, V., Mees, F. (Eds.), Interpretation of Micromorphological Features of Soils and Regoliths. Elsevier, Amsterdam, pp. 149–194.

Dypvik, H., Harris, N.B., 2001. Geochemical facies analysis of fine-grained siliciclastics using Th/U, Zr/Rb and (Zr+ Rb)/Sr ratios. Chem. Geol. 181 (1–4), 131–146.

Egeland, C.P., Gasparian, B., Fadem, C.M., Nahapetyan, S., Arakelyan, D., Nicholson, C.M., 2016. Bagratashen 1, a stratified open-air Middle Paleolithic site in the Debed river valley of northeastern Armenia: a preliminary report. Archaeol. Research in Asia 8, 1–20.

Eglinton, G., Hamilton, R.J., 1967. Leaf epicuticular waxes. Science 156, 1322–1335.

Eley, Y.L., Hren, M.T., 2018. Reconstructing vapor pressure deficit from leaf wax lipid molecular distributions. Sci. Rep. 8, 1–8.

Eren, M.I., Boehm, A.R., Morgan, B.M., Anderson, R., Andrews, B., 2011. Flaked stone taphonomy: a controlled experimental study of the effects of sediment consolidation on flake edge morphology. J. Taphonomy 9, 201–217.

Fleitmann, D., Cheng, H., Badertscher, S., Edwards, R.L., Mudelsee, M., Göktürk, O.M., Fankhauser, A., Pickering, R., Raible, C.C., Matter, A., Kramers, J., Tüysüz, O., 2009. Timing and climatic impact of Greenland interstadials recorded in stalagmites from northern Turkey. Geophys. Res. Lett. 36, 1–5.

Folk, R.L., Ward, W.C., 1957. Brazos River bar [Texas]; a study in the significance of grain size parameters. J. Sediment. Res. 27 (1), 3–26.

Frahm, E., Schmidt, B.A., Gasparyan, B., Yeritsyan, B., Karapetian, S., Meliksetian, K., Adler, D.S., 2014. Ten seconds in the field: rapid Armenian obsidian sourcing with portable XRF to inform excavations and surveys. J. Archaeol. Sci. 41, 333–348.

Frahm, E., Feinberg, J.M., Schmidt-Magee, B.A., Wilkinson, K.N., Gasparyan, B., Yeritsyan, B., Adler, D.S., 2016. Middle Palaeolithic toolstone procurement behaviors at Lusakert cave, Hrazdan valley, Armenia. J. Hum. Evol. 91, 73–92.

Friedman, I., Smith, R.L., Long, W.D., 1966. Hydration of natural glass and formation of perlite. Geol. Soc. Am. Bull. 77, 323–328.

Galván, B., Hernández, C.M., Mallol, C., Mercier, N., Sistiaga, A., Soler, V., 2014. New evidence of early neandertal disappearance in the iberian peninsula. J. Hum. Evol. 75, 16–27.

Gasparyan, B., Egeland, C.P., Adler, D.S., Pinhasi, R., Glauberman, P., Haydosyan, H., 2014. The Middle paleolithic occupation of Armenia: summarizing old and new data. In: Gasparyan, B., Arimura, M. (Eds.), Stone Age of Armenia: Guide-Book to the Stone Age Archaeology in the Republic of Armenia. Center for Cultural Resource Studies, Kanazawa University, Kanazawa, pp. 65–106.

Gevorgyan, H., Repstock, A., Schulz, B., Meliksetian, K., Breitkreuz, C., Israyelyan, A., 2018. Decoding a post-collisional multistage magma system: the quaternary ignimbrites of Aragats stratovolcano, western Armenia. Lithos 318, 267–282.

Ghukasyan, R., Colonge, D., Nahapetyan, S., Ollivier, V., Gasparyan, B., Monchot, H., Chataigner, C., 2011. Kalavan-2 (north of Lake Sevan, Armenia): a new late Middle paleolithic site in the lesser Caucasus. Archaeol. Ethnol. Anthropol. Eurasia 38, 39–51.

Gifford-Gonzalez, D.P., Damrosch, D.B., Damrosch, D.R., Pryor, J., Thunen, R.L., 1985. The third dimension in site structure: an experiment in trampling and vertical dispersal. Am. Antiq. 50, 803–818.

Gill, R., 2010. Igneous Rocks and Processes: a Practical Guide. Blackwell, UK.

Gile, L.H., Peterson, F.F., Grossman, R.B., 1966. Morphological and genetic sequences of carbonate accumulation in desert soils. Soil Sci. 101 (5), 347–360.

Glauberman, P.J., Thorson, R.M., 2012. Flint patina as an aspect of "flaked stone taphonomy": a case study from the loess terrain of The Netherlands and Belgium. J. Taphonomy 10, 21–43.

Glauberman, P., Gasparyan, B., Wilkinson, K., Frahm, E., Raczynski-Henk, Y., Haydosyan, H., Arakelyan, D., Karapetyan, S., Nahapetyan, S., Adler, D., 2016. Introducing Barozh 12: a Middle palaeolithic open-air site on the edge of the Ararat depression, Armenia. ARAMAZD-Armenian J. Near Eastern Studies IX, 7–20.

Golovanova, L.V., Doronichev, V.B., 2003. The Middle palaeolithic of the Caucasus. J. World PreHistory 17, 71–140.

Groucutt, H.S., Scerri, E.M., Lewis, L., Clark-Balzan, L., Blinkhorn, J., Jennings, R.P., Parton, A., Petraglia, M.D., 2015. Stone tool assemblages and models for the dispersal of Homo sapiens out of Africa. Quat. Int. 382, 8–30.

Hammer, Ø., Harper, D.A., Ryan, P.D., 2001. PAST: Paleontological statistics software package for education and data analysis. Palaeontologia Electronica 4, 1–9, 4.

Hauck, T.C., 2011. Mousterian technology and settlement dynamics in the site of Hummal (Syria). J. Human Evol. 61, 519–537.

Heiri, O., Lotter, A.F., Lemcke, G., 2001. Loss on ignition as a method for estimating organic and carbonate content in sediments: reproducibility and comparability of results. J. Paleolimnol. 25 (1), 101–110.

Hovers, E., Ekshtain, R., Greenbaum, N., Malinsky-Buller, A., Nir, N., Yeshurun, R., 2014. Islands in a stream? Reconstructing site formation processes in the late Middle Paleolithic site of 'Ein Qashish, northern Israel. Quat. Int. 331, 216–233.

Jerram, D., Petford, N., 2011. The Field Description of Igneous Rocks, 2nd. John Wiley & Sons, Chichester.

Jetter, R., Kunst, L., Samuels, A.L., 2006. Composition of plant cuticular waxes. In: Riederer, M., Miller, C. (Eds.), Biology of the Plant Cuticle. Blackwell Publishing Ltd, Oxford, pp. 145–181.

Jones, A.P., Tucker, M.E., Hart, J., 1999. The description & analysis of quaternary stratigraphic field sections, 7. Quaternary Research Association.

Karapetian, S.G., Jrbashian, R.T., Mnatsakanian, A.K., 2001. Late collision rhyolitic volcanism in the northeastern part of the Armenian highland. J. Volcanol. Geoth. Res. 112, 189–220.

Krajcarz, M.T., Gola, M.R., Cyrek, K.J., 2010. Preliminary suggestions on the Pleistocene palaeovegetation around the Bisnik Cave (Czestochowa Upland, Poland) based on studies of molecular fossils from cave sediments. Stud. Quat. 27, 55–61.

Klein, R.G., 1966. Chellean and acheulean on the territory of the soviet union: a critical review of the evidence as presented in the Literature. Am. Anthropol.: New Series 68, 1–45.

Kühn, P., 2003. Micromorphology and late glacial/holocene genesis of Luvisols in mecklenburg–vorpommern (NE-Germany). Catena 54 (3), 537–555.

Kuman, K., Field, A.S., 2009. The Oldowan industry from Sterkfontein Caves, South Africa. In: Schick, K., Toth, N. (Eds.), The cutting edge: New approaches to the archaeology of human origins. Stone Age Institute Press, Indiana, pp. 151–169.

Lebedev, V.A., Chernyshev, I.V., Yukashev, A.I., 2011. Initial time and duration of quaternary magmatism in the Aragats neovolcanic area (lesser Caucasus, Armenia). Dokl. Earth Sci. 437, 532–536.

Lebedev, V.A., Chernyshev, I.V., Shatagin, K.N., Bubnov, S.N., Yakushev, A.I., 2013. The Quaternary volcanic rocks of the Geghama Highland, Lesser Caucasus, Armenia: geochronology, isotopic Sr–Nd characteristics, and origin. J. Volcanol. Seismol. 7, 204–229.

Leierer, L., Jambrina-Enríquez, M., Herrera-Herrera, A.V., Connolly, R., Hernández, C.M., Galván, B., Mallol, C., 2019. Insights into the timing, intensity and natural setting of Neanderthal occupation from the geoarchaeological study of combustion structures: a micromorphological and biomarker investigation of El Salt, unit Xb, Alcoy, Spain. PloS One 14 (4), e0214955.

Lericolais, G., Popescu, I., Guichard, F., Popescu, S.M., Manolakakis, L., 2007. Water-level fluctuations in the Black Sea since the last glacial maximum. In: The Black Sea Flood Question: Changes in Coastline, Climate, and Human Settlement. Springer, Dordrecht, pp. 437–452.

Li, F., Kuhn, S.L., Chen, F.Y., Gao, X., 2016. Raw material economies and mobility patterns in the Late Paleolithic at Shuidonggou locality 2, north China. J. Anthropol. Archaeol. 43, 83–93.

Li, H., Li, Z.Y., Lotter, M.G., Kuman, K., 2018. Formation processes at the early Late Pleistocene archaic human site of Lingjing, China. J. Archaeol. Sci. 96, 73–84.

Lindbo, D.L., Stolt, M.H., Vepraskas, M.J., 2010. Redoximorphic features. In: Stoops, G., Marcelino, V., Mees, F. (Eds.), Interpretation of Micromorphological Features of Soils and Regoliths. Elsevier, Amsterdam, pp. 129–147.

Lisiecki, L.E., Raymo, M.E., 2005. A Pliocene-Pleistocene stack of 57 globally distributed benthic d18O records. Paleoceanography 20, PA1003. https://doi.org/10.1029/2004PA001071.

Litt, T., Pickarski, N., Heumann, G., Stockhecke, M., Tzedakis, P.C., 2014. A 600,000 year long continental pollen record from Lake Van, eastern Anatolia (Turkey). Quat. Sci. Rev. 104, 30–41.

Lotter, M.G., Gibbon, R.J., Kuman, K., Leader, G.M., Forssman, T., Granger, D.E., 2016. A geoarchaeological study of the middle and upper Pleistocene levels at Canteen Kopje, Northern Cape Province, South Africa. Geoarchaeology 31, 304–323.

McBrearty, S., Bishop, L., Plummer, T., Dewar, R., Conard, N., 1998. Tools underfoot: human trampling as an agent of lithic artifact edge modification. Am. Antiq. 63, 108–129.

McPherron, S.P., Braun, D.R., Dogandžić, T., Archer, W., Desta, D., Lin, S.C., 2014. An experimental assessment of the influences on edge damage to lithic artifacts: a consideration of edge angle, substrate grain size, raw material properties, and exposed face. J. Archaeol. Sci. 49, 70–82.

Meignen, L., Tushabramishvili, N., 2006. Paléolithique moyen laminaire sur les flancs sud du Caucase: productions lithiques et fonctionnement du site de Djruchula, Géorgie. Paleorient 32, 81–104.

Mitchell, J., Westaway, R., 1999. Chronology of Neogene and Quaternary uplift and magmatism in the Caucasus: constraints from K–Ar dating of volcanism in Armenia. Tectonophysics 304, 157–186.

Moncel, M.-H., Pleurdeau, D., Tushabramishvili, N., Yeshurun, R., Agapishvili, T., Pinhasi, R., Higham, T.F.G., 2013. Preliminary results from the new excavations of the Middle and upper palaeolithic levels at ortvale klde-north chamber (south Caucasus Georgia). Quat. Int. 316, 3–13.

Moncel, M.-H., Pleurdeau, D., Pinhasi, R., Yeshurun, R., Agapishvili, T., Chevalier, T., Lebourdonnec, F.-X., Poupeau, G., Nomade, S., Jennings, R., Higham, T., Tushabramishvili, N., Lordkipanidze, D., 2015. The Middle palaeolithic record of Georgia: a synthesis of the technological, economic and paleoanthropological aspects. Anthropol. Lit. III (1 -2), 93–125.

Nash, D.T., Petraglia, M.D., 1987. Natural formation processes and the archaeological record, 352. British Archaeological Reports, Oxford.

Nielson, A., 1991. Trampling the archaeological record: an experimental study. Am. Antiq. 56, 483–503.

Panichkina, M.Z., 1950. In: Iessen, A.A. (Ed.), Paleolit Armenii/Paleolithic of Armenia. State Hermitage Press, Leningrad (in Russian).

Pei, S., Niu, D., Guan, Y., Nian, X., Kuman, K., Bae, C.J., Gao, X., 2014. The earliest late paleolithic in North China: site formation processes at Shuidonggou locality 7. Quat. Int. 347, 122–132.

Petraglia, M.D., Potts, R., 1994. Water flow and the formation of early Pleistocene artifact sites in olduvai gorge, Tanzania. J. Anthropol. Archaeol. 13, 228–254.

Philip, H., Cisternas, A., Gvishiani, A., Gorshkov, A., 1989. The Caucasus: an actual example of the initial stages of continental collision. Tectonophysics 161, 1–21.

Pickarski, N., Kwiecien, O., Djamali, M., Litt, T., 2015. Vegetation and environmental changes during the last interglacial in eastern Anatolia (Turkey): a new high-resolution pollen record from Lake Van. Palaeogeogr. Palaeoclimatol. Palaeoecol. 435, 145–158.

Poch, R.M., Artiedo, O., Herrero, J., Verba-Lebedeva, M., 2010. Micromorphology of gypsic features in soils and sediments. In: Stoops, G., Marcelino, V., Mees, F. (Eds.), Interpretation of Micromorphological Features of Soils and Regoliths. Elsevier, Amsterdam, pp. 195–216.

Pryor, J.H., 1988. The effects of human trample damage on lithics: a consideration of crucial variables. Lithic Technol. 17, 45–50.

Pustovoytov, K.E., 2002. Pedogenic carbonate cutans on clasts in soils as a record of history of grassland ecosystems. Palaeogeogr. Palaeoclimatol. Palaeoecol. 177, 199–214.

Pustovoytov, K., 2003. Growth rates of pedogenic carbonate coatings on coarse clasts. Quat. Int. 106, 131–140.

Randlett, M.-E., Bechtel, A., van der Meer, M.T.J., Peterse, F., Litt, T., Pickarski, N., Kwiecien, O., Stockhecke, M., Wehrli, B., Schubert, C.J., 2017. Biomarkers in Lake Van sediments reveal dry conditions in eastern Anatolia during 110.000-10.000 years B.P. G-cubed 18, 571–583.

Röttlander, R.C.A., 1975. the formation of patina on flint. Archaeometry 17, 106–110.

Sardaryan, S.H., 1954. Paleolit v armenii/paleolithic in Armenia. In: Hastratyan, M.A. (Ed.), Armenian SSR Academy of Sciences Press: Yerevan (in Russian).

Sayyed, M.R.G., Hundekari, S.M., 2006. Preliminary comparison of ancient bole beds and modern soils developed upon the Deccan volcanic basalts around Pune (India): potential for palaeoenvironmental reconstruction. Quat. Int. 156, 189–199.

Schick, K.D., 1984. Processes of Palaeolithic Site Formation: an Experimental Study. Unpublished PhD Dissertation, University of California, Berkeley.

Schick, K.D., 1986. Stone Age Sites in the Making: Experiments in the Formation and Transformation of Archaeological Occurrences, vol. 319. British Archaeological Reports, Oxford.

Schick, K.D., 1987. Experimentally-derived criteria for assessing hydrologic disturbance of archaeological sites. In: Nash, D.T., Petraglia, M.D. (Eds.), Natural Formation Processes and the Archaeological Record, British Archaeological Reports 352: Oxford, pp. 86–107.

Schiffer, M.J., 1983. Towards the identification of formation processes. Am. Antiq. 48, 675–705.

Schimmelmann, A., Lewan, M.D., Wintsch, R.P., 1999. D/H isotope ratios of kerogen, bitumen, oil, and water in hydrous pyrolysis of source rocks containing kerogen types I, II, IIS, and III. Geochem. Cosmochim. Acta 63, 3751–3766.

Schlanger, S.H., 1992. Recognizing persistent places in anasazi settlement systems. In: Rossignol, J., Wandsnider, L. (Eds.), Space, Time, and Archaeological Landscapes. Springer, New York, pp. 91–112.

Sheldon, N.D., Tabor, N.J., 2009. Quantitative paleoenvironmental and paleoclimatic reconstruction using paleosols. Earth Sci. Rev. 95 (1–2), 1–52.

Sitzia, L., Bertran, P., Boulogne, S., Brenet, M., Crassard, R., Delagnes, A., Frouin, M., Hatte', C., Jaubert, J., Khalidi, L., Messager, E., Mercier, N., Meunier, A., Peigne', S., Queffelec, A., Tribolo, C., Macchiarelli, R., 2012. The paleoenvironment and lithic taphonomy of Shi'Bat dihya 1, a Middle palaeolithic site in wadi surdud, Yemen. Geoarchaeology 27, 471–491.

Snyder, J.A., Wasylik, K., Fritz, S.C., Wright, J., 2001. Diatom-based conductivity reconstruction and palaeoclimatic interpretation of a 40-ka record from Lake Zeribar, Iran. Holocene 11, 737–745.

Srivastava, P., Sangode, S.J., Meshram, D.C., Gudadhe, S.S., Nagaraju, E., Kumar, A., Venkateshwarlu, M., 2012. Paleoweathering and depositional conditions in the inter-flow sediment units (bole beds) of Deccan Volcanic Province, India: a mineral magnetic approach. Geoderma 177, 90–109.

Stockhecke, M., Timmermann, A., Kipfer, R., Haug, G.H., Kwiecien, O., Friedrich, T., Menviel, L., Litt, T., Pickarski, N., Anselmetti, F.S., 2016. Millennial to orbital-scale variations of drought intensity in the Eastern Mediterranean. Quat. Sci. Rev. 133, 77–95.

Thiry, M., Fernandes, P., Milnes, A., Raynal, J.P., 2014. Driving forces for the weathering and alteration of silica in the regolith: implications for studies of prehistoric flint tools. Earth Sci. Rev. 136, 141–154.

Thomsen, K.J., Murray, A.S., Jain, M., Botter-Jensen, L., 2008. Laboratory fading rates of various luminescence signals from feldspar-rich sediment extracts. Radiat. Meas. 43, 1474–1486.

Toomanian, N., Jalalian, A., Eghbal, M.K., 2001. Genesis of gypsum enriched soils in north-west Isfahan, Iran. Geoderma 99, 199–224.

Toomanian, N., Jalalian, A., Eghbal, M.K., 2003. Application of the WRB (FAO) and US taxonomy systems to gypsiferous soils in Northwest Isfahan, Iran. J. Agric. Sci. 5, 51–66.

Treadwell-Steitz, C., McFadden, L.D., 2000. Influence of parent material and grain size on carbonate coatings in gravelly soils, Palo Duro Wash, New Mexico. Geoderma 94 (1), 1–22.

Ünal-İmer, E., Shulmeister, J., Zhao, J.-X., Uysal, I.T., Feng, Y.-X., Nguyen, A.D., Yüce, G., 2015. An 80 kyr-long continuous speleothem record from Dim Cave, SW Turkey with paleoclimatic implications for the Eastern Mediterranean. Sci. Rep. 5, 13560.

Van Vliet-Lanoë, B., Magyari, A., Meilliez, F., 2004. Distinguishing between tectonic and periglacial deformations of Quaternary continental deposits in Europe. Global Planet. Change 43 (1–2), 103–127.

Vermeersch, P.M., Bubel, S., 1997. Postdepositional artefact scattering in a podzol. Processes and consequences for late palaeolithic and mesolithic sites. Anthropologie XXXV/2, 119–130.

Volodicheva, N., 2002. The Caucasus. In: Shahgedanova, M. (Ed.), The Physical Geography of Northern Eurasia. Oxford University Press, Oxford, pp. 350–376.

Wegwerth, A., Kaiser, J., Dellwig, O., Shumilovskikh, L.S., Nowaczyk, N.R., Arz, H.W., 2016. Northern hemisphere climate control on the environmental dynamics in the glacial Black Sea "Lake". Quat. Sci. Rev. 135, 41–53.

Wolf, D., Baumgart, P., Meszner, S., Fülling, A., Haubold, F., Sahakyan, L., Meliksetian, K., Faust, D., 2016. Loess in Armenia–stratigraphic findings and palaeoenvironmental indications. Proc. Geologists' Assoc. 127, 29–39.

Yamnova, I.A., 1990. Gypsiferous Soils of the Dzhizak Steppe. Proceedings of Soil Sciences Institute Moscow, pp. 37–39.